Crustal Magmatic System Beneath the East Pacific Rise (8°20' to 10°10'N): Implications for Tectonomagmatic Segmentation and Crustal Melt Transport at Fast-Spreading Ridges

Milena Marjanović, Suzanne M. Carbotte, Hélène D. Carton, Mladen R. Nedimović, Juan Pablo Canales, John C. Mutter

AGU100 ADVANCING EARTH AND SPACE SCIENCE

Geochemistry, Geophysics, Geosystems

RESEARCH ARTICLE
10.1029/2018GC007590

Key Points:
- The 2-D and 3-D swath seismic data sets are used to characterize crustal magmatic system beneath the East Pacific Rise from 8°20′ to 10°10′N
- Disruptions in continuity of magma lenses are observed and in places are vertically aligned indicating coincident magmatic segmentation
- Observations support the hypothesis that third-order segments represent volcanic/magmatic units extending from seafloor to uppermost mantle

Supporting Information:
- Supporting Information S1
- Figure S1
- Figure S2
- Figure S3
- Figure S4
- Figure S5

Correspondence to:
M. Marjanović,
marjanovic@ipgp.fr

Citation:
Marjanović, M., Carbotte, S. M., Carton, H. D., Nedimović, M. R., Canales, J. P., & Mutter, J. C. (2018). Crustal magmatic system beneath the East Pacific Rise (8°20′ to 10°10′N): Implications for tectonomagmatic segmentation and crustal melt transport at fast-spreading ridges. *Geochemistry, Geophysics, Geosystems*, *19*, 4584–4611. https://doi.org/10.1029/2018GC007590

Received 3 APR 2018
Accepted 29 OCT 2018
Accepted article online 6 NOV 2018
Published online 23 NOV 2018

Crustal Magmatic System Beneath the East Pacific Rise (8°20′ to 10°10′N): Implications for Tectonomagmatic Segmentation and Crustal Melt Transport at Fast-Spreading Ridges

Milena Marjanović[1], Suzanne M. Carbotte[2], Hélène D. Carton[1], Mladen R. Nedimović[2,3], Juan Pablo Canales[4], and John C. Mutter[2]

[1]Equipe de Géosciences Marines, Institut de Physique du Globe de Paris, Sorbonne Paris Cité, Paris, France, [2]Department of Marine Geology and Geophysics, Lamont-Doherty Earth Observatory, Palisades, NY, USA, [3]Department of Earth Sciences, Dalhousie University, Halifax, Nova Scotia, Canada, [4]Department of Geology and Geophysics, Woods Hole Oceanographic Institution, Woods Hole, MA, USA

Abstract Detailed images of the midcrustal magmatic system beneath the East Pacific Rise (8°20′–10°10′N) are obtained from 2-D and 3-D-swath processing of along axis seismic data and are used to characterize properties of the axial crust, cross-axis variations, and relationships with structural segmentation of the axial zone. Axial magma lens (AML) reflections are imaged beneath much of the ridge axis (mean depth 1,640 ± 185 m), as are deeper sub-AML (SAML) reflections (brightest events ~100–800 m below AML). Local shallow regions in the AML underlie two regions of shallow seafloor depth from 9°40′–55′N and 8°26′–33′N. Enhanced magma replenishment at present beneath both sites is inferred and may be linked to nearby off-axis volcanic chains. SAML reflections, which are observed primarily from 9°20′ to 10°05′N, indicate a finely segmented magma reservoir similar to the AML above, composed of subhorizontal, 2- to 7 km-long AML segments, often with stepwise changes in reflector depth from one segment to the next. We infer that these melt bodies are related to short-lived melt instability zones. In many locations including where seismic constraints are strongest the intermediate scale (~15–40 km) structural segmentation of the ridge axis identified in this region coincides with (1) changes in average thickness of layer 2A (by 10%–15%), (2) changes in average depth of AML (<100 m), and (3) with the spacing of punctuated low velocity zones mapped in the uppermost mantle. The ~6 km dominant length of multiple AML segments within each of the larger structural segments may reflect the spacing of local sites of ascending magma from discrete melt reservoirs pooled beneath the crust.

1. Introduction

Much of what is known about the architecture of the magmatic system beneath fast spreading mid-ocean ridges (MOR) is derived from active-source seismic studies, which reveal the presence of a thin (tens to hundreds of meters), relatively narrow (<1 km) lens of magma located in the shallow crust. This magma lens extends for many tens of kilometers above a broader zone of low seismic velocities that are attributed to melt in the lower crust and shallowest mantle (Carbotte et al., 2000, 2013; Detrick et al., 1987; Dunn et al., 2000; Hooft et al., 1997; Kent et al., 1993a, 1994; Singh et al., 1998, 2006; Toomey et al., 2007; VanderBeek et al., 2016; Vera et al., 1990). Melts from this system feed the dike intrusions and volcanic eruptions that build the upper crust, while in situ cooling and crystallization leads to the formation of the gabbroic section that makes up the lower crust (e.g., Natland & Dick, 2001; Sinton & Detrick, 1992). An important question in MOR studies is how the distribution of melt beneath the ridge axis detected in seismic studies is related to the structural segmentation of the ridge observed at the seafloor. Structural segmentation at fast-spreading ridges is observed on a range of scales defined by offsets of the axial zone ranging from transform faults with offsets typically >30 km to smaller nontransform offsets that have a variety of forms (e.g., Haymon et al., 1991; Macdonald et al., 1988). Observations of systematic gradients in ridge properties or of common geochemical characteristics along the sections of ridge between these offsets led to the hypothesis that these structural or tectonic segments reflect segmentation within the underlying magma plumbing system (e.g., Langmuir et al., 1986; Macdonald et al., 1988; Sinton et al., 1991). Long-standing questions include whether the different scales of tectonic segments correspond with magma supply centers and what depths and processes

beneath the MOR contribute to spatial variations in melt distribution (e.g., Carbotte et al., 2015, and references therein). Early models proposed that the largest-scale tectonic segmentation arises from subcrustal processes, linked to variations in mantle source composition or mantle melting and transport processes, whereas the finest-scale segmentation was hypothesized to reflect shallow crustal processes, linked to dike intrusion and eruption (e.g., Langmuir et al., 1986; Macdonald et al., 1988). Other early models proposed that tectonic discontinuities along spreading centers form in response to changes of spreading direction (e.g., Lonsdale, 1989). The contribution of mantle versus lithosphere processes to the different scales of segmentation continues to be debated and strong feedbacks are expected. Recent models based on observations from fast-spreading ridges and ophiolite analogs include (1) those that primarily involve mantle melting and transport (e.g., diapiric melt ascent (Le Mée et al., 2004), and small upper mantle melt heterogeneities, Gomez & Briais, 2000); (2) those that invoke mantle/lithosphere interactions (e.g., skewness in mantle flow and influence on plate boundary reorganziation, Toomey et al., 2007; VanderBeek et al., 2016), melt focusing due to lithosphere thickness gradients (Gregg et al., 2007; Hebert & Montési, 2011), influence of plate boundary migration on melt production, and melt focusing due to lithosphere gradients (Carbotte et al., 2004; Katz et al., 2004); and (3) those that pertain to finer-scale segmentation and involve crustal processes (e.g., hydrothermal circulation cells within the upper crust, Fontaine et al., 2011; Tolstoy et al., 2008, and convection within crustal magma reservoirs, Fontaine et al., 2017).

The East Pacific Rise (EPR) bounded by the Clipperton and Siqueiros TF has been a region of focused investigation for >30 years (e.g., Fornari et al., 2012, and references therein). All scales of tectonic segmentation are identified here and much of our understanding of ridge processes at fast spreading rates derives from the numerous geochemical, geophysical, and geologic studies conducted in the region. Following the hierarchical classification scheme of Macdonald et al. (1988), the length of ridge between the Clipperton and Siqueiros TFs is defined as a first-order segment and is subdivided by a large-offset overlapping spreading center (OSC) centered at 9°03′N into two second-order segments, each further subdivided into numerous smaller third- and fourth-order segments (Haymon et al., 1991; Macdonald et al., 1991). Early observations of regional gradients in ridge properties north of the 9°03′N OSC led to the hypothesis of a long-term mantle magma supply center located beneath this ~120-km long segment with along-axis melt flow redistributing melt away from this region (e.g., Barth & Mutter, 1996; Scheirer & Macdonald, 1993; Wang et al., 1996). More recent observations argue against this model and indicate more closely spaced sites of mantle magma delivery to and in the crust. For example, the seismic tomography study of the uppermost mantle beneath the ridge axis extending from the Clipperton to the Siqueiros TFs reveals the presence of many discrete low velocity zones (attributed to higher melt concentrations) beneath the larger-scale tectonic segments (Toomey et al., 2007). The spacing (15–35 km) of these subcrustal regions of higher melt concentration (1%–3%) is comparable to that of the intermediate scale, that is, third-order seafloor structural segmentation found in this region. Based on *ARGO* near-bottom sonar data and imagery (Fornari et al., 1998; Haymon et al., 1991), White et al. (2002) found systematic variations in lava morphology indicating gradients in lava effusion rates as well as other seafloor properties within these structural segments. These results led White et al. (2000, 2002) to propose that this third-order of segmentation corresponds with the predominant volcanic/magmatic segments along the EPR, each fed by a common magma plumbing system.

In 2008, multistreamer, multisource, multichannel seismic data were acquired over the EPR between the Clipperton and Siqueiros TFs, including a series of cross-axis lines from ~9°38′ to 58′N designed for high resolution 3-D imaging centered on a region of recent volcanic eruption at 9°46′–56′N (Cowen et al., 2007; Fundis et al., 2010; Rubin et al., 2012; Soule et al., 2007; Tan et al., 2016; Tolstoy et al., 2006) as well as a series of along-axis lines providing regional coverage of the axial zone from ~8°20′ to 10°10′N (Figure 1a). Analyses of the seismic data (Aghaei et al., 2014; Canales et al., 2012; Carbotte et al., 2012, 2013; Han et al., 2014; Marjanović et al., 2014, 2015; Mutter et al., 2008; Xu et al., 2014) show that while a bright axial magma lens (AML) reflection is present beneath much of the ridge axis, it is discontinuous on a fine scale and that disruptions in the AML reflection coincide in many places with the fine-scale discontinuities in the seafloor axial fissure zone (Carbotte et al., 2013). Structural variations in the AML including steps and local deeps in the AML reflector, diminished reflectivity, and/or presence of reflector complexities define discrete ~5- to 15-km long magma lens segments that are well aligned with the fine-scale seafloor tectonic segmentation. A recent high-resolution velocity study of upper crustal seismic velocities, using the same along-axis data, reveals quasi-vertical low-velocity zones inferred to be upgoing and downgoing pathways of hydrothermal

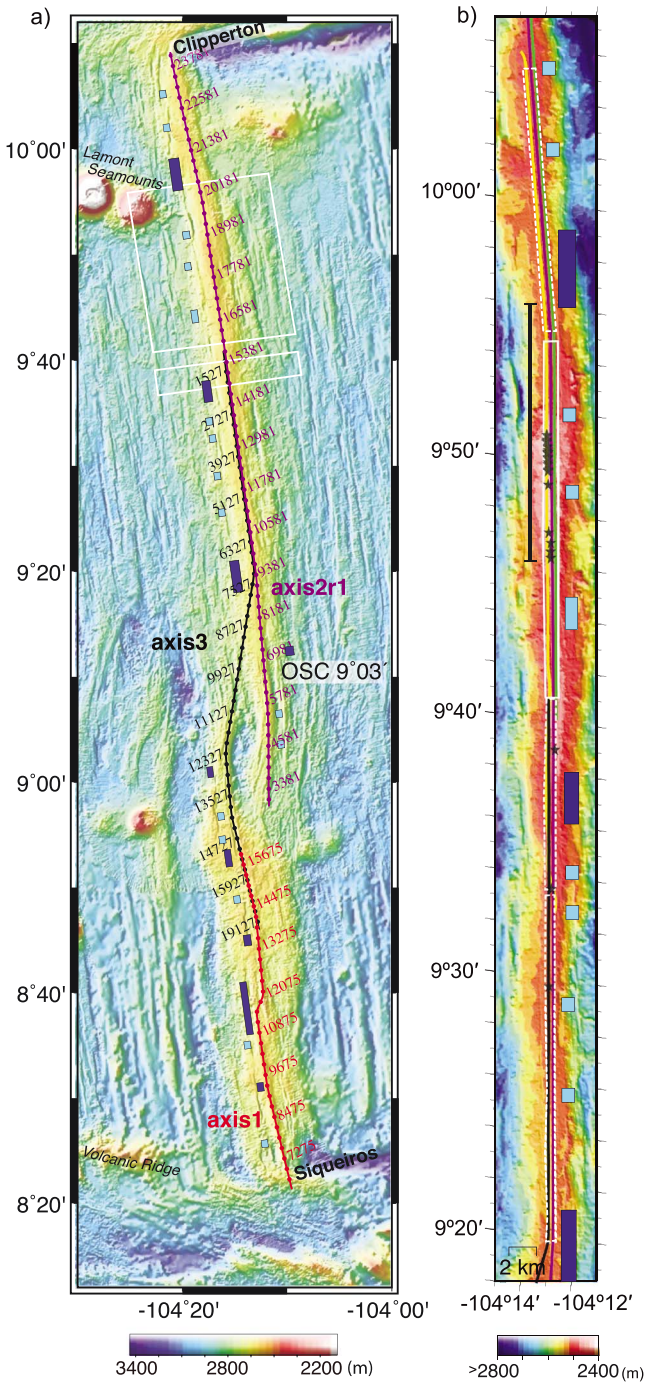

Figure 1. (a) Location of multichannel seismic (MCS) data sets collected during expedition MGL0812, aboard R/V *M. G. Langseth*. Tracks of the along-axis profiles used for 2-D data processing are shown in red (axis1), black (axis3), and purple (axis2r1) lines with dots marking location of every 300 common midpoints (CMPs) along each line (every 1200 CMP is indicated by a number). White rectangles outline the extent of the cross-axis 3-D volumes (Aghaei et al., 2014; Han et al., 2014). The underlying seafloor bathymetry map is a composite map prepared from the Global Multi-Resolution Topography (GMRT) synthesis (Ryan et al., 2009) and multibeam sonar data acquired during the cruise gridded at 50 m, with tectonic discontinuities of the ridge axis indicated: Siqueiros and Clipperton transform faults, overlapping spreading center (OSC) at 9°03′N, and third- and fourth-order discontinuity zones marked in dark and light blue rectangles, respectively (Carbotte et al., 2013; White et al., 2006). (b) Location of the along-axis MCS data set processed as a 3-D swath. Extent of the 3-D migrated data is shown in white rectangles (dashed and solid); combined axis-centered inlines shown in Figure A1 are extracted from the box in white solid rectangle. Colored lines show location of the 2-D sail lines used for 3-D processing: yellow—axis3p2, purple—axis2r1, black—axis3, and green—axis4. The underlying seafloor bathymetry map is a composite map prepared from the data acquired during the MGL0812 cruise and the data from White et al. (2006) gridded at 30 m. Location of hydrothermal vent sites (Fornari et al., 2012) are marked in black stars; the along-axis extent of the lava flow (Soule et al., 2007) emplaced during the 2006 eruption (Tan et al., 2016) is indicated with a black bar. The third- and fourth-order discontinuities are marked as in (a).

flow within the 9°50′N region (Marjanović et al., 2017). From the location of the imaged low-velocity anomalies, presence of molten AML segments (Marjanović et al., 2015), and higher-order tectonic discontinuities, which are zones of likely higher upper crustal permeability, the study argues that regional high thermal regime (sourced from an AML segment), spatially and temporally correlated with high permeability zones within the crust, is needed to develop, maintain, and drive vigorous, high-temperature hydrothermal flow. In addition, Marjanović et al. (2015) conducted an analysis of melt content variation along the ridge axis and find that melt content varies within AML segments at much smaller spatial scales (as small as ~100 m). This study also examined relationships between AML melt content variation at these small scales and the distribution of abundant high-temperature hydrothermal venting found in the region, where individual vent sites are spaced at ~200 m (Fornari et al., 2012; Haymon et al., 1991; Von Damm, 1995, 2000, 2004). This study shows that individual vent sites do not necessarily sit directly above the most molten pockets of the AML.

In addition to defining physical properties of the AML and the upper crust, the collected seismic sections reveal the presence of deeper, subaxial magma lenses (SAMLs) indicating a magmatic system beneath the AML composed of vertically stacked sills, which may extend through the entier lower crust (Marjanović et al., 2014).

In the current study, along-axis 2-D and 3-D swath data acquired during the 2008 experiment (Figure 1) are used to further investigate the characteristics of the crustal magmatic system including the AML, the recently seismically imaged SAML events, and the uppermost crustal layer, seismic layer 2A, and relationships with seafloor structural segmentation. Of particular interest are the properties of the shallow crustal magma system within third-order tectonic segments (intermediate scale of segmentation), which have been hypothesized to represent primary accretionary units. Multiple, closely spaced along-axis sail lines acquired from ~9°20′ to 10°10′N are processed as a 3-D swath imaging a region 500- to 800-m-wide centered at the axis, and providing constraints on the cross-axis thickening of layer 2A and the plan view geometry of the AML and underlying SAMLs. Two-dimensional analysis using the sail lines acquired to follow the axial eruptive fissure zone provide constraints on the zero-age thickness of layer 2A, and on the depth and distribution of the underlying AML and SAML events over the larger region between the Siqueiros and Clipperton TFs. To examine relationships between tectonic and magmatic segmentation, average properties and along-axis variations are examined for the different structural segments identified in the region. Key findings of our study pertain to the geometry of the SAMLs, which are found to be even more finely segmented than the AML above. The results provide new insights concerning the depths at which magma bodies reside in the crust, the origin of the fine- to intermediate-scale segmentation of the AML and SAMLs, and the relationships with the current distribution of melt in the uppermost mantle previously imaged beneath this stretch of the EPR.

2. Tectonic Segmentation of the EPR 8°20′–10°10′N

Our study region extends ~220 km along the EPR from the Siqueiros TF in the south to the Clipperton TF in the north (Figure 1a). Within this area, an ~5.5- to 7.3-km thick oceanic crust is accreted (Aghaei et al., 2014; Barth & Mutter, 1996; Canales et al., 2003) at an average full spreading rate of 108–109 mm/year (Carbotte & Macdonald, 1992). From the numerous sonar and seafloor photo studies conducted in the region, the morphology of the axial zone and the location of tectonic discontinuities are well mapped (e.g., Fornari et al., 1998; Haymon et al., 1991; Macdonald et al., 1988, 1991; Soule et al., 2009; White et al., 2002, 2006). The 9°03′N OSC is a major nontransform discontinuity expressed as a wide zone along the ridge axis where two overlapping ridges (by 27 km) are offset by up to 8 km. Following the criteria of Macdonald et al. (1991) and White et al. (2000), nine intermediate-scale discontinuities of the ridge axis are found in the region that correspond with small (0.5- to 2-km wide and ~1.2- to 9.5-km long) OSCs or lateral steps in the axial summit trough (AST, Fornari et al., 1998), which encompasses the zone of modern fissuring and eruption (Figure 1a; White et al., 2006). The third-order segments between these discontinuities range in length from 12 to 38 km. Smaller changes in ridge axis orientation and/or steps in the AST of $<$0.5 km define the finest-scale (fourth-order) tectonic segmentation of the ridge (Carbotte et al., 2013; Haymon et al., 1991; Macdonald et al., 1988, 1991; White et al., 2006). Different interpretations of the location of these finest-scale discontinuities in our study area have been presented in the literature based largely on the quality of

sonar mapping data available at the time; here we adopt the identification of White et al. (2006) with minor modifications by Carbotte et al. (2013). The length of the fourth-order structural segments defined by the finest-scale discontinuities ranges from 2 to 14 km in our study region.

As observed elsewhere along the EPR, systematic variations in the depth and width or cross-sectional area of the ridge axis are observed that are closely associated with the structural segmentation. Discontinuities are typically coincident with local deeps and minima in axial depth and cross-sectional area and have been attributed to disruptions in the magmatic system (Macdonald et al., 1991; Scheirer & Macdonald, 1993). In our study area, the 9°03′N OSC is associated with an axial depth anomaly of 100–150 m**,** depth anomalies of $>$20 m are associated with the third-order discontinuities, and those associated with the finest-scale discontinuities are negligible (Scheirer & Macdonald, 1993; White et al., 2002). A regional gradient in axial depth is observed along the second-order segment north of the OSC that corresponds with density variations on-axis and is attributed to a gradient in crustal compositions with more Fe-rich compositions due to higher degrees of magmatic differentiation to the south (Toomey & Hooft, 2008).

Constraints on the longevity of the structural segmentation in the region come from a regional-scale magnetic study which shows a V-shaped migration trace for the 9°03′N OSC marked by a highly magnetized crust extending at least to the past 2 Ma (Carbotte & Macdonald, 1992). This study indicates that the smaller 9°37′N and 8°37′N third-order discontinuities are also long-lived features ($>$780 kyr; Plate 2, Carbotte & Macdonald, 1992). High-resolution crustal thickness data from 9°42′ to 57′N acquired during our survey indicates variations in the character of the Moho reflection and variability of crustal thickness consistent with the persistence of segmentation assocaited with the small 9°51.3′N offset over the past ~180 kyr (Aghaei et al., 2014). Regional-scale but lower resolution crustal thickness studies indicate locally thinner crust associated with the zone of abandoned overlap basins and ridges on the flanks of the 9°03′N discontinuity (Barth & Mutter, 1996; Canales et al., 2003). Notably, the thickest crust within the region from the Siqueiros to Clipperton TF is found ~15-km north of the OSC, centered from 9°10′ to 9°20′N in near-ridge (~70–150 kyr) crust and coincides with the denser crust inferred in the study of Toomey and Hooft (2008). This local zone is part of a V-shaped band of thicker crust that extends farther on the ridge flanks (Figure 9 in Canales et al., 2003) and tracks the zone of high magnetization (Plate 2 in Carbotte and Macdonald, 1992), marking the long-term southward propagation of the 9°03′N discontinuity.

3. Data and methods

3.1. Seismic Experiment and Data Processing

The multichannel seismic (MCS) data used in this study were acquired with the R/V *M. G. Langseth* using two tuned air-gun arrays fired in flip-flop mode, each composed of two strings of nine guns, with a total volume of 3,300 in^3. The source was deployed at 7.5 m below the sea surface and shot at an interval of 37.5 m. The signal was recorded using four solid state 6 km long streamers, each with 468 channels, spaced at 12.5 m (the first channel ~200 m from the source). Using these four streamers spaced at 150 m, together with alternating shooting mode we obtain eight across-track common midpoint (CMP) lines. Therefore, each ship track or sail line resulted in eight CMP profiles spaced 37.5 m apart and an in-line CMP spacing of 6.25 m, covering a subsurface swath of 300 m or more, depending on streamer feathering.

During the survey five along-axis sail lines, which are the focus of this study, were collected providing coverage of the entire ridge segment from the Clipperton to Siqueiros TFs (Figure 1). They include three neighboring parallel sail lines between 10°10′ and 9°41′N (axis3p2, axis2r1, and axis4), two from 9°41′ to 9°20′N (axis2r1 and axis3), one line extending from 9°20′N and over the eastern limb of the 9°03′ OSC (axis2r1), and one two-part sail line from 9°20′ to 8°20′N extending over the western limb of the 9°03′N OSC (axis1 and axis3). For the sail lines axis1, axis2r1, and axis3 the streamers were deployed at 7.5 m below the sea surface, whereas for sail lines axis3p2 and axis4 they were at 10 m (Mutter et al., 2008). Throughout most of the study area, the seismic lines closely follow the location and azimuth changes of the modern ridge axis, except for ~30 km along the eastern limb of the 9°03′N OSC.

The along-axis data were processed assuming a nominal 2-D geometry, by combining into a single profile two CMP lines collected using one of the inner streamers (exhibiting higher signal to noise ratio and minimal lateral offset to the source) and shots from both air-gun arrays (thus resulting in a CMP fold of 78). For the

Table 1
Processing Sequence for Along-Axis 2-D Line and 3-D Swath Data Sets

Processing sequence	Line (CBL#2)	Swath
Geometry definition	2-D geometry	3-D geometry
Editing	Bad channels excluded and interpolated	Bad channel excluded and interpolated
Prestack	1. Band-pass filtering 2–7–220–250 Hz	1. Band-pass filtering: 2–7–220–250 Hz
	2. Spherical divergence correction	2. Suppress swell noise and spherical divergence correction
	3. Surface consistent amplitude correction	4. f-k filter
	4. Resampling to 4 ms (with applied antialiasing filter) and 8-s trace length	5. Resample at 4 ms (with antialiasing filter applied) and 8-s trace length
	5. Edits applied	6. Edits applied
	6. Mute right above the first water multiple	7. Flexible binning (bins = 6.25 × 37.5 m) with maximum fold = 39
		8. Surface consistent amplitude correction
		9. Mute right above the first water multiple
Stacking	7. Defining stacking velocity	10. Defining 3-D velocity function for stacking (V3-D)
	8. NMO and stacking	11. NMO and stack CMP gathers using V3-D velocity
Poststack	9a. Layer 2A: 2-D Kirchhoff poststack time migration using 90% of the ESP5	15a. Layer 2A: 2-D Kirchhoff poststack time migration using 90%V3D
	9b. AML: 2-D Kirchhoff poststack time migration using ~80% of the ESP5	15b. AML: 2-D Kirchhoff poststack time migration using ~80% V3D
Display	10. Top mute above the seafloor	16. Top mute above the seafloor
	11. Apply surgical mute to the layer 2A section and merge it with the AML section	17. Scaling entire 2-D swath
	12. Scaling composite seismic section	

Note. The processing flow(s) were designed for optimal imaging of the following crustal events: seafloor, layer 2A, AML, and SAML. AML = axial magma lens; SAML = sub-AML; NMO = normal-move out; CMP = common midpoint; ESP5 = expanded spread profile 5.

region north of 9°20′N, where multiple neighboring sail lines were shot, the data were also processed as 3-D swaths taking into account the true 3-D geometry (Figure 1b).

The prestack processing sequence for the 2-D seismic analysis includes geometry definition, application of band-pass filter, spherical divergence correction and surface consistent amplitude correction, f-k filtering, data editing, resampling to 4 ms, and muting of the first water multiple and below (see Table 1 for processing parameters used). Using the prestack data, we perform velocity analysis, which we use to apply normal-move out (NMO) correction and stack the data. From velocity analysis of the AML reflection event using semblance, and examination of constant velocity stacks, we find that the AML and SAML events throughout most of our survey area are well imaged with a stacking velocity of 2,500 ± 50 m/s, except in the vicinity of the 9°03′N OSC where a higher stacking velocity (2,600 m/s) for the AML event is required. Results from this analysis are used to modify root-mean-square velocities derived from the expanded spread profile 5 velocity function of Vera et al. (1990; obtained on-axis at 9°34.4′N). The obtained velocity function is then hung from the seafloor and used for stacking the seafloor, AML, and SAML events (the resulting sections are referred to here as the AML section). For stacking the layer 2A event, we approximately follow the procedure described in Carbotte et al. (2000). Optimal stacking velocities for the layer 2A event are determined from evaluation of constant velocity stacks for a range of velocities from 1,530 to 1,700 m/s and using midrange source-receiver offsets of 1,500–3,000 m. Layer 2A stacks best using 1,580 m/s for the region south of the OSC 9°03′N, and 1,560 m/s for north of the OSC. Higher velocities of 1,680 m/s are required to optimally stack the event within the OSC region. The section that is stacked with the above velocities and offset range is hereinafter referred to as the layer 2A section.

The poststack processing sequence includes 2-D Kirchhoff time migration for collapsing diffractions and reposition dipping events, applied to both sections (AML and layer 2A) separately. After migrating the layer 2A section, we apply a surgical mute to extract the event and merge it with the AML section to obtain the final seismic image (e.g., Nedimović et al., 2008; Figure 2).

The 3-D processing was conducted using lines axis2r1, axis3, axis3p2, and axis4 (Figure 1b), following a processing sequence very similar to that for the 2-D profiles, as described above and outlined in Table 1. The main difference lies in geometry definition at the preprocessing stage. To process the 3-D data, inline/crossline CMP bin grids (*boxes*) are defined, one for each section where the orientation of the

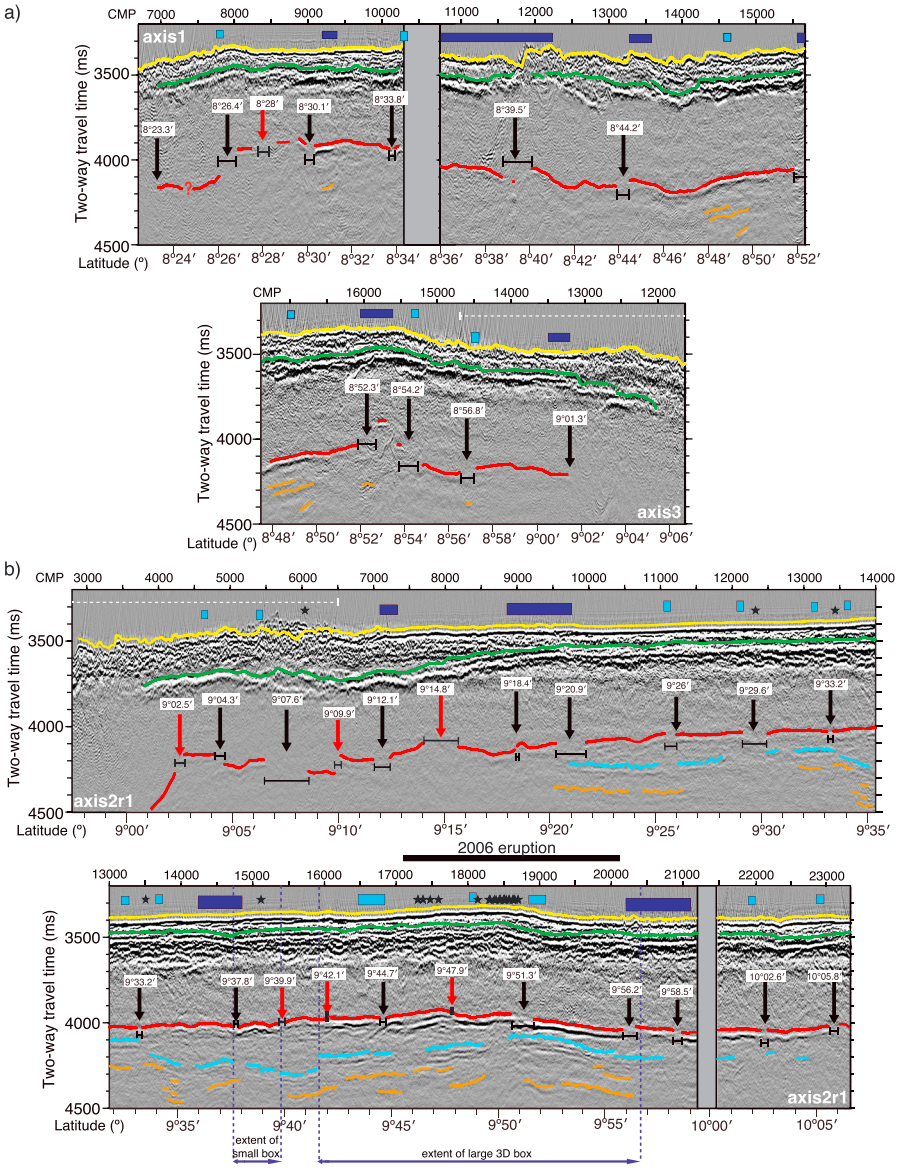

Figure 2. (a) Migrated seismic sections (axis1 on top panel and axis3 on bottom panel) along the southern second-order segment with two-way traveltime (twtt) picks superimposed for the seafloor (yellow), layer 2A (green), axial magma lens (AML) (red), and potential sub-AMLs (SAMLs; orange). All picks are shifted ~10 ms above the corresponding event for better visibility of the seismic horizon. Locations of mapped AML interruptions that are within 1 km of a tectonic discontinuity identified in the seafloor above are indicated with black arrows (with latitude labeled); the ones that are more than 1 km from the nearest discontinuity are marked in red. Horizontal black bars show the lateral extent of the AML interruption zones. Gray area without seismic data represents location of low fold data excluded from further analysis. Tectonic discontinuities are shown in dark, and light blue horizontal bars to denote third- and fourth-order discontinuities in bathymetry, respectively. Dashed white bar shows latitudinal extent of seafloor discontinuity zone delimiting the extent of the overlapping spreading center (OSC) 9°03′N. (b) Migrated seismic section (profile axis2r1) along the northern second-order segment with digitized seafloor (yellow), layer 2A (green), AML (red), shallow SAML (blue), and deeper/potential SAML (orange) picks, superimposed. Black stars indicate location of vent sites (Von Damm, 2000; Fornari et al., 2012), and black bar above the lower panel shows the extent of the lava flow emplaced during the 2006 eruption (Soule et al., 2007; Tan et al., 2016). Remaining symbols, bars, and arrows are the same as in (a). Blue arrows represent along-axis extent of cross-axis 3-D boxes shown in Figure 1a.

seismic line remains approximately constant, parallel to the ridge crest. We define a total of three boxes, with transitions between boxes associated with a change in line orientation of approximately 1° (Figure 1b). Details on geometry definition and shot selection are given in Marjanović (2013). Flexible binning and

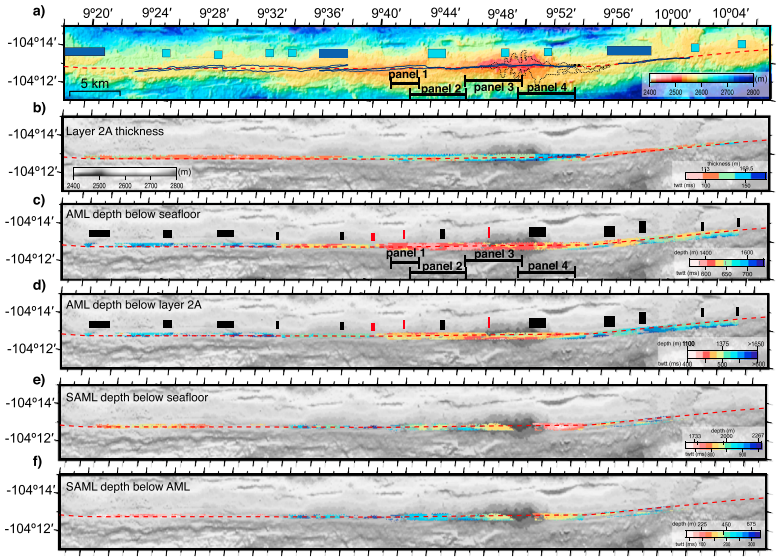

Figure 3. (a) Plan view of composite EM300 bathymetry from White et al. (2006) and EM120 multibeam sonar data acquired during the MGL0812 cruise with location of seismic 2-D line (red dashed line), and along-axis extent of third- (dark blue rectangles) and fourth-order (light blue rectangles) tectonic discontinuities, superimposed. Dotted line shows mapped extent of the lava flow from the 2006 eruption (from Soule et al., 2007), and dark blue lines outline the extent of the axial summit trough (Escartín et al., 2007; Fornari et al., 1998; Soule et al., 2009). Remaining panels show plan view of twtt/depth-converted horizons digitized from 3-D swath data north of 9°20′N superimposed on gray shaded bathymetry: (b) layer 2A two-way traveltimes (twtt)/thickness, (c) axial magma lens (AML) twtt/depth below seafloor, (d) AML twtt/depth below layer 2A, (e) SAML twtt/depth below seafloor, (f) sub-AML (SAML) twtt/depth below AML. In panels (c) and (d), black/red boxes show extent of AML disruptions that are located less than or equal to versus greater than 1 km of a discontinuity identified in the seafloor above respectively. In (a) and (c), horizontal bars indicate latitudinal extent of four panels shown in Figure 7: panel 1-7d), panel 2-7c), panel 3-7b), and panel 4-7a).

regularization are additional processing steps that are not part of the 2-D prestack processing sequence. The flexible binning reorganizes the data into CMP bins of 37.5 × 6.25 m with 39 traces in each CMP bin, corresponding to the nominal fold (Yilmaz, 2001). The stacking sequence follows that used for the 2-D profiles. For the seafloor, AML and SAML events, NMO correction is applied using a 3-D velocity function derived from the modified expanded spread profile 5 velocity function used for 2-D processing. This velocity is hung from the seafloor bathymetry grid for each box. Data stacking follows the application of NMO correction. Poststack time migration is carried out in 3-D. As for the 2-D lines, we stack and migrate the layer 2A event separately.

3.2. Mapping Crustal Events

Along the lines processed in 2-D, the primary seismic horizons, including seafloor, layer 2A, AML, and SAML (where present), are digitized using a semi-automated picking tool. Digitized picks are filtered using a zero-phase filter to remove short-wavelength noise associated with the semi-automated picking. For each of the horizons, we tested different filter window widths and used 150 m for the seafloor, 600 m for layer 2A, and 300 m for both AML and SAML. For all events except layer 2A, we pick the first minimum of the wavelet (trough of the first white on seismic sections displayed in Figure 2). For layer 2A, the first maximum (peak of the first black) of the wavelet is picked, as this is the most prominent phase of this wavelet. Uncertainties in two-way traveltimes (twtt) for the digitized horizons arise from the picking uncertainties (±8 ms), filtering (±6 ms), and from the uncertainties associated with velocities used for stacking of the interpreted horizons. Exploring the range of possible stacking velocities needed to optimally image each of the seismic horizons, we estimate stacking errors of ±16 ms for layer 2A and SAML, and ±8 ms for AML and seafloor.

Seismic horizons from the 3-D swath volumes located north of 9°20′N were digitized using a voxel-tracking tool (Figure 3). The same phases of the events are picked as for the data analyzed in 2-D. Estimated uncertainties in digitized events are as for the data processed in 2-D.

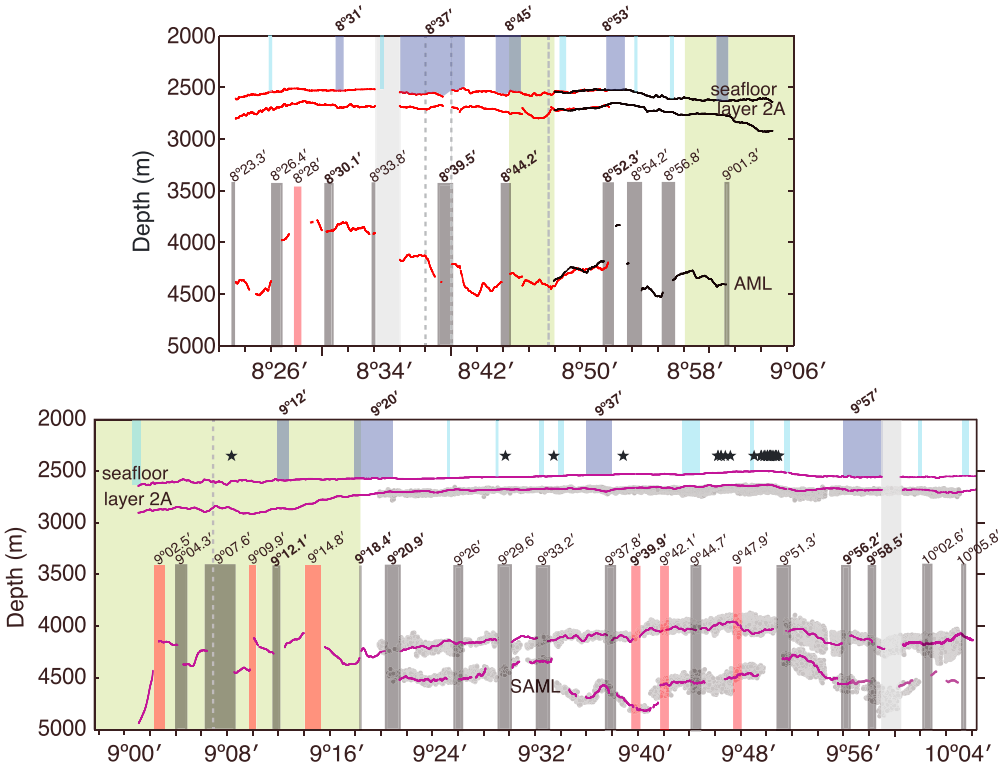

Figure 4. Depth-converted seismic horizons: seafloor, layer 2A, axial magma lens (AML) and sub-AMLs (SAMLs). Picks from axis1 and axis3 are shown in red and black, respectively, on top panel, and picks from axis2r1 are shown in purple on bottom panel (locations are shown in Figure 1a). Horizons were picked from migrated seismic sections (Figure 2) and depth converted using velocity functions explained in the text. Third- and fourth-order tectonic discontinuities are marked above the seafloor using dark and light blue shaded zones, respectively. The latitude of the center of each third-order tectonic discontinuity is labeled. Identified interruptions in the AML reflector that are within 1 km of a tectonic discontinuity identified in the seafloor above are shown in black vertical bars; the AML disruptions that are located >1 km from the nearest discontinuity are shown in red box. The latitude of the center of each disruption is labeled (in bold for disruptions interpreted to correspond with third-order tectonic discontinuities). Gray zone spanning the layer 2A, AML, and SAML picks along the axis2r1 profile (bottom panel) correspond with picks from the equivalent layers mapped within the 500- to 800-m wide along-axis 3-D swath and projected to the axial line (Figure 3). Vertical dashed gray zones show locations of large (>10°) azimuthal changes in the survey lines, and the green shaded regions represent areas where the seismic profiles were >300 m away from the axial zone. Black stars show locations of hydrothermal vent sites (Von Damm, 2000; Fornari et al., 2012).

The crustal traveltimes for all events, mapped along the 2-D lines and 3-D swath volumes, are converted to depth (Figures 3 and 4) using constant layer velocities appropriate for the axial region (2,260 m/s for layer 2A and 5,500 m/s for layer 2B from Vera et al., 1990). For depth conversion of the SAMLs below the AML, a constant velocity of 4,500 m/s estimated from the velocity model of Dunn et al. (2000) is used. Using these constant velocities for depth conversion, the combined picking, filtering, and stacking errors translate to uncertainties of approximately ±25 m for layer 2A, ±38 m for AML and ±50 m for the shallowest SAML. In addition, a constant velocity assumption for depth conversion introduces further uncertainty. If we assume a range of velocities and average twtt thickness of 2,250–2,500 m/s and ~130 ms for layer 2A, and 5,200–5,400 m/s (Marjanović et al., 2017) and ~500 ms for layer 2B, maximum uncertainties in AML depth are up to 65 m. Given the poor constraints on crustal velocities below the AML (e.g., Collier & Singh, 1997; Xu et al., 2014), absolute depth uncertainties up to ~200 m are estimated for the SAML (derived assuming velocities ranging from 4,500 to 5,500 m/s). In addition to the shallowest SAML events, along 2-D lines we also identify deeper SAMLs on 2-D lines (Figures 2 and S1a and S1b in the supporting information), but due to their low signal-to-noise ratio, their traveltime/depth information and related uncertainty are poorly constrained and properties of these weak events beyond their distribution are not further examined.

In the Appendix, we provide a short discussion on assessing imaging differences between 2-D line and 3-D swath by comparing horizons picks obtained along the 2-D line and horizons picked in the coincident line extracted from 3-D swath.

4. Observations on Crustal Structure

In the following section observations of along-axis variations in the continuity, depth, and geometry of the layer 2A, AML, and SAML events, and how these variations relate to seafloor structural segmentation are described. The 2-D transects, which approximately follow the axial eruptive fissure zone for the EPR between Siqueiros and Clipperton TF (Escartín et al., 2007; Fornari et al., 1998; Fornari et al., 2004; Schouten et al., 1999; Soule et al., 2005), are used to characterize the structure along the axis, while the 3-D swath data provide constraints on both axial and cross-axis structure for the region north of 9°20′N. Properties of the AML, SAML, and layer 2A events beneath seafloor discontinuities are examined. In particular, average properties and along-axis variations are examined with respect to seafloor depth, an indicator of structural segmentation (e.g., Scheirer & Macdonald, 1993; Figure 5 and Table 2). For characterization of properties associated with the finest-scale seafloor segmentation, we limit our analysis to the region north of 9°20′N where 3-D swath data coverage is available, as this scale of segmentation is best resolved in this region. Note that throughout the paper we use the terms *northern segment* and *southern segment* to refer to the length of the ridge north and south of the 9°03′N OSC to the Clipperton and Siqueiros TFs, respectively. These correspond to second-order segments in the classification of Macdonald et al. (1988).

4.1. Layer 2A Characteristics

4.1.1. Two-Dimensional Lines—Axial Structure

A bright horizon from the base of seismic layer 2A is present beneath almost the full length of the axis in this region (Figures 2 and 4) at an average depth of 165 ± 40 metres below seafloor (mbsf; 145 ± 30 ms twtt) measured along the 2-D axially centered line. The thickest layer 2A is found in the vicinity of the 9°03′N OSC, reaching up to three times the regional average toward the ends of both overlapping ridge limbs. This thickening is likely to be due, in part, to the location of our seismic line, which is situated up to 1 km away from the axial fissure zone (Figure 1a), and hence is likely sampling the thicker layer 2A typically found off-axis along the EPR (Carbotte et al., 1997; Harding et al., 1993; Kent et al., 1994; Vera & Diebold, 1994).

Outside of the OSC region, layer 2A is thinner and more uniform in thickness along the ridge to the north (average thickness 140 ± 35 m north of 9°12′N) than to the south (170 ± 25 m, Table 2). The small changes in layer 2A thickness found along the northern segment coincide with several seafloor discontinuities. These include a local thickening to 175 m within the discontinuity zone of the small OSC centered at 9°37′N (Smith et al., 2001; Figures 2b and 4), where our ship track is well aligned with the modern ridge axis (Figure 1). A change from a near-uniform thickness to gradual southward thickening occurs at the 9°20′N discontinuity (Figure 2b). A local thickening (by several tens of meters) is also found north of the smaller seafloor discontinuities mapped at 9°51.8′N and 10°02′N.

Along the southern segment, the layer 2A event is more complex and variable in depth (Figure 2a). There are several locations where multiple and/or dipping events are observed, including from 8°41′ to 8°43′N, and in the vicinity of seafloor discontinuities at 8°53′N, and 8°48.5′N. At other places, seafloor discontinuities coincide with changes in layer 2A thickness, as observed on the northern segment. The 9°01′N discontinuity coincides with a change from a more uniform layer 2A thickness to the south to a more discontinuous layer 2A event and gradual thickening to the north. A change in layer 2A thickness is observed crossing the small OSC centered at 8°37′N with a locally thicker layer 2A along the northern OSC limb (Figures 2a and 4).

Over the length of ridge imaged in our study, there is no correlation between layer 2A thickness and seafloor depth (Figure 5). While a thicker layer 2A is found where the seafloor is deeper along the northern segment, we also see the full range of layer 2A thickness variation, from ~100 to 250 m at the shallowest seafloor depths (2,500–2,550 m). There are small differences in the thickness of layer 2A between many adjacent third-order structural segments, but most are less than estimated uncertainties (Table 2).

4.1.2. Three-Dimensional Swath—Across-Axis Structure

In the along-axis 3-D swath data (Figure 3b), three prominent near stepwise changes in layer 2A thickness are observed that occur at 9°37′N (up to 40 m), 9°56′N (up to 60 m) and near 9°51.8′N (up to 60 m). These stepwise changes are present across the width of the swath, and all coincide with tectonic discontinuities (the

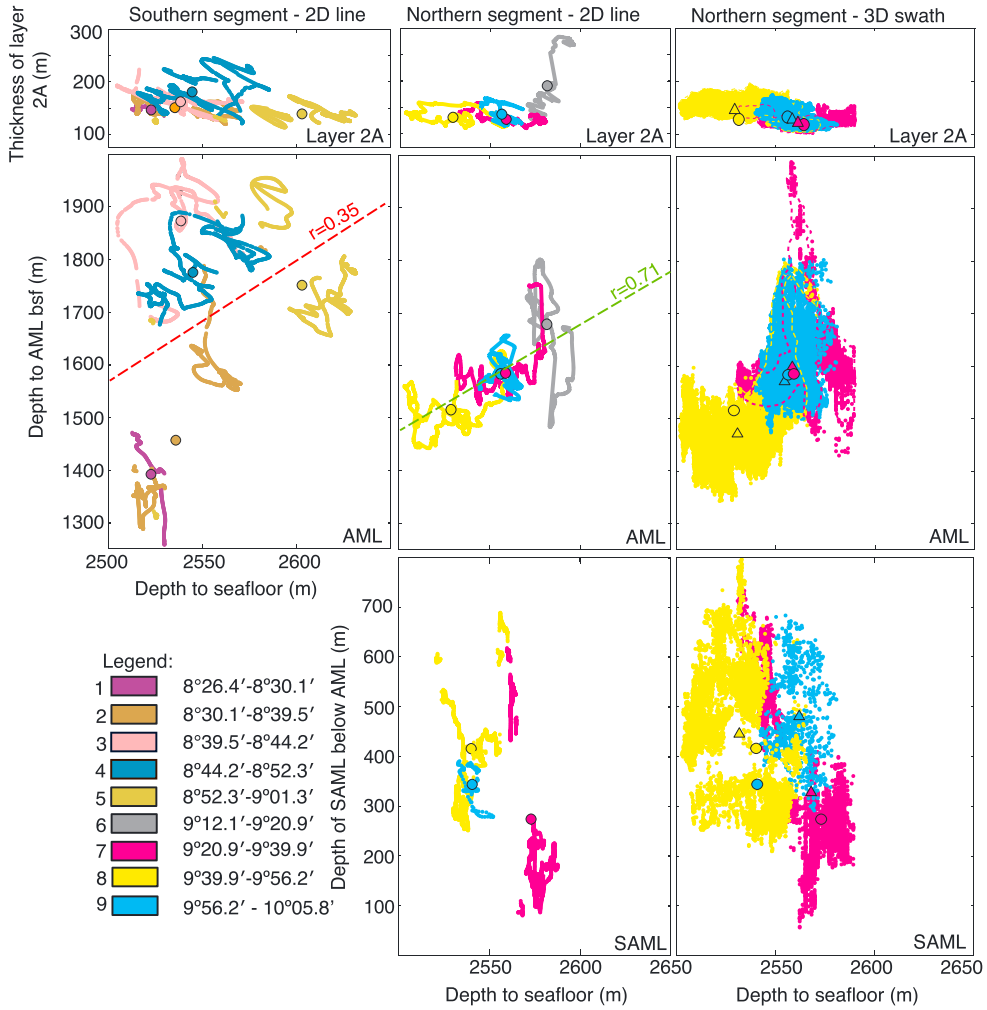

Figure 5. Scatterplots of crustal horizons mapped from the 2-D and 3-D swath seismic data sets. From top to bottom, plots show layer 2A thickness against seafloor depth (top), depth of axial magma lens (AML) below seafloor against seafloor depth (middle), and sub-AML (SAML) depth below the AML against seafloor depth (restricted to the area north of 9°20′N) for all identified third-order tectonic segments mapped along the southern (left) and northern (middle) 2-D profiles, and within the 3-D swath (right). The extents of the third-order segments are as defined in Table 2 and color-coded as explained in the legend. For the northern segment we exclude picks south of 9°12′N as our seismic line deviates significantly from the identified axis within much of this region. Colored circles indicate mean values of the variables for each segment mapped in 2-D; colored triangles (right panels) are used to indicate mean values obtained from the 3-D swath. Dashed lines represent the best fit linear trend with correlation coefficient indicated for the southern (red) and northern (green) second-order segment. In the right hand panels, for the regions where the data points overlap, dashed lines contour the hidden part of the data clouds. The differences in SAML picks at shallowest seafloor depths from the 2-D line versus the 3-D swath reflect the better imaging with the 2-D axial line due to higher fold (78 for 2-D line compared to 39 in the swath) and hence higher signal-to-noise ratio.

9°37′ and 9°57′ third-order offset zones and the finer-scale offset at 9°51.8′N). Between these tectonic discontinuities layer 2A is nearly uniform in thickness. Small but significant differences in average thickness (by 10–15%) are measured for the three adjacent intermediate-scale structural segments imaged in the region of 3-D swath coverage (Table 2).

For most of the imaged region, there is little across-axis thickening of layer 2A (up to few tens of meters on each side; Figure 3b). However, within the zone extending between 9°42′ and 9°54′N, which roughly coincides with the region of documented recent eruptions, a somewhat greater thickening in the across-axis direction is found (up to 50 m), which is consistent with this site being the location of more frequent eruptions that breach and extend away from the AST. An asymmetry in across-axis thickening of layer 2A that

Geochemistry, Geophysics, Geosystems

10.1029/2018GC007590

Table 2

Average Depths (with Standard Deviations) of Crustal Horizons Layer 2A, AML Below Seafloor, and Shallowest SAML Below AML Mapped from 2-D Along-axis Lines and 3-D Swath Within Second-, Third-, and Fourth-order Tectonic Segments and Interpreted Corresponding Magmatic Segments

Segment order	Ridge axis discontinuity (degrees latitude)	Tectonic segment (degrees latitude)	AML segment/ group of segments (degrees latitude)	Layer 2A twtt bsf (ms)/thickness (m)		AML twtt (ms)/depth (m) bsf		SAML below AML twtt (ms)/depth (m)	
				2-D line	3-D swath	2-D line	3-D swath	2-D line	3-D swath
Southern segment 2nd order	8°23′ (Siqueiros) OSC 9°03′N	8°23′–9°03′	8°26.4–9°01.3	150 ± 20/170 ± 25	_	700 ± 70/1,685 ± 185	_	_	_
Northern segment 2nd order	OSC 9°03′N	9°03′–10°09.5′	9°01.2′–10°5.8′ (9°12′–10°5.8′)&	140 ± 50/160 ± 55 (125 ± 30/140 ± 30)	_	665 ± 60/1,600 ± 110 (645 ± 35/1,575 ± 70)	_	_	_
	10°09.5 (Clipperton)								
Southern segment third-order	8°23′ (Siqueiros) 8°31′	8°23′-31′	8°26.4–30.1′	130 ± 5/145 ± 5	—	585 ± 25/1,400 ± 65	—	—	—
	8°37′ (36′-41′)	8°31′-38.5′	8°30.1–39.5′	140 ± 10/155 ± 10	—	610 ± 45/1,450 ± 130	—	—	—
	8°45′ (44.5′-45.5′)	8°38.5–45′	8°39.5–44.2′	155 ± 15/175 ± 15	—	765 ± 30/1,860 ± 85	—	—	—
	8°53′ (52′-53.5′)	8°45′-53′	8°44.2–52.3′	170 ± 20/195 ± 25	—	730 ± 30/1,740 ± 55	—	—	—
	9°01′ (00.5′-01.5′)	8°53′-9°01′	8°52.3–9°01.3′	135 ± 10/155 ± 10	—	710 ± 50/1,735 ± 130	—	—	—
Northern segment third-order	9°12′ (12′-12.8)	9°12′-20′	9°12.1–20.9′	170 ± 45/190 ± 50	—	710 ± 20/1,680 ± 85	—	—	—
	9°20′ (18′-21′)	9°20′-9°37′	9°20.9–39.9′	120 ± 5/130 ± 10	110 ± 10/125 ± 10	640 ± 15/1,585 ± 40	650 ± 30/1,575 ± 50	120 ± 75/275 ± 165	155 ± 60/350 ± 130
	9°37′ (36′-38′)	9°37′-57.5′	9°39.9–56.2′	120 ± 10/130 ± 10	130 ± 15/150 ± 20	620 ± 15/1,515 ± 40	610 ± 15/1,475 ± 35	185 ± 50/415 ± 110	200 ± 40/445 ± 95
	9°57′ (56′-59′) 10°09.5 (Clipperton)	9°57.5′-10°09.5′	9°56.2–10°5.8′	125 ± 15/140 ± 15	115 ± 10/135 ± 15	650 ± 10/1,585 ± 25	650 ± 20/1,600 ± 45	150 ± 75/344 ± 65	215 ± 40/480 ± 90
Northern segment fourth-order	9°25.5′	9°20–25.5′	9°20.9–26′	110 ± 5/125 ± 5	110 ± 10/130 ± 10	660 ± 20/1,630 ± 50	690 ± 10/1,605 ± 20	80 ± 20/180 ± 40	130 ± 15/295 ± 30
	9°29′	9°25.5–29′	9°26–29.6′	110 ± 5/125 ± 5	105 ± 10/120 ± 10	640 ± 5/1585 ± 10	670 ± 20/1,580 ± 65	85 ± 15/190 ± 30	100 ± 10/225 ± 25
	9°32.5′	9°29–32.5′	9°29.6–33.2′	105 ± 5/120 ± 5	100 ± 5/115 ± 5	630 ± 5/1560 ± 15	690 ± 30/1,635 ± 95	65 ± 10/140 ± 20	100 ± 10/225 ± 15
	9°34.1′	9°32.5′-34.1′							
	9°37 (36′-38′)	9°34.1–37′	9°33.2′-37.8′	115 ± 10/130 ± 10	110 ± 10/125 ± 10	635 ± 5/1555 ± 20	625 ± 10/1,540 ± 15	195 ± 60/435 ± 135	230 ± 40/520 ± 90
		_	9°37.8–39.9′	125 ± 5/140 ± 5	125 ± 10/145 ± 10	650 ± 5/1580 ± 20	640 ± 5/1,560 ± 10	255 ± 20/570 ± 40	275 ± 20/6,205 ± 50

Geochemistry, Geophysics, Geosystems

10.1029/2018GC007590

Table 2 *(continued)*

Segment order	Ridge axis discontinuity (degrees latitude)	Tectonic segment (degrees latitude)	AML segment/ group of segments (degrees latitude)	Layer 2A twtt bsf (ms)/thickness (m)		AML twtt (ms)/depth (m) bsf		SAML below AML twtt (ms)/depth (m)	
				2-D line	3-D swath	2-D line	3-D swath	2-D line	3-D swath
	9°37 (36′-38′)[a]								
	_	_	9°39.9–42.1′	115 ± 5/130 ± 5	130 ± 10/145 ± 10	615 ± 10/1,510 ± 20	610 ± 5/1,475 ± 15	270 ± 40/600 ± 95	300 ± 20/670 ± 50
	9°44′ (43.5′-44.7′)	9°37′-44′	9°42.1–44.7′	110 ± 10/125 ± 10	130 ± 15/145 ± 15	605 ± 5/1480 ± 10	600 ± 5/1,455 ± 15	190 ± 10/425 ± 20	240 ± 15/540 ± 30
	9°48.8′	9°44′-48.8′	9°44.7–47.9′	110 ± 5/125 ± 5	130 ± 10/145 ± 10	600 ± 5/1470 ± 20	600 ± 5/1,450 ± 45	160 ± 15/365 ± 40	230 ± 30/520 ± 65
	9°51.8′	9°48.8′-51.8′	9°47.9–51.3′	120 ± 5/140 ± 5	135 ± 20/155 ± 20	630 ± 10/1,530 ± 20	615 ± 5/1,460 ± 20	135 ± 10/305 ± 30	180 ± 25/400 ± 55
	9°57 (56′-59′)	9°51.8–57′	9°51.3–56.2′	120 ± 15/135 ± 15	140 ± 20/160 ± 20	635 ± 10/1,550 ± 50	625 ± 10/1,510 ± 45	180 ± 45/410 ± 100	170 ± 25/380 ± 55
	9°57 (56′-59′)[a]	_	9°56.2–58.5′	110 ± 5/130 ± 5	110 ± 10/120 ± 10	630 ± 5/1560 ± 15	630 ± 10/1,565 ± 20	275 ± 10/620 ± 20	200 ± 30/440 ± 70
	10°02′	9°57′-10°02′	9°58.5–10°02.6′	110 ± 5/120 ± 5	120 ± 10/130 ± 10	650 ± 10/1,615 ± 15	650 ± 15/1,615 ± 45	155 ± 10/350 ± 25	230 ± 45/520 ± 100
	10°05.2′	10°02–10°05.2	10°02.6′-10°5.8′	140 ± 5/160 ± 5	150 ± 15/170 ± 10	655 ± 5/1575 ± 10	665 ± 20/1,630 ± 50	170 ± 5/380 ± 5	—

Note. Along the northern second-order segment we give the average depths for the entire segment as well as for region north of 9°12′N, given that our seismic line deviates significantly from the axis in the OSC region. AML = axial magma lens; SAML = sub-AML; twtt = two-way travel times; bsf = below seafloor.
[a]Third-order seafloor discontinuity (latitude range) which spans AML segment.

changes sense along the eruption zone is also apparent: north of ~9°51.8′N and south of ~9°46′N, layer 2A is thicker to the west implying sustained preferential accumulation of lavas to the west, while from ~9°46′–51.8′, it is thicker on the eastern flank (Figure 3b).

4.2. AML Characteristics

4.2.1. Two-Dimensional Lines—Axial Structure

A seismic reflection from the AML is imaged along ~85% of the ridge axis extending between the Siqueiros and Clipperton TFs, at a mean depth of 1,640 ± 185 m below the seafloor with a maximum depth range of over 800 m (from 1,310 to 2,150 m) observed along the axis-centered 2-D profile. On average the AML is shallower and less variable in depth beneath the northern second-order segment (Figures 4 and 5). However, locally, the shallowest AML events are observed beneath the ridge axis south of the 9°03′N OSC, centered at ~8°53′N (~1,310 mbsf) and ~8°30′N (~1,380 mbsf). The shallow event at 8°53′N extends for only 0.6 km beneath the axis and underlies a small volcanic cone (~300 m in width and 20 m in height) found within the wide AST present in this region (Figure S2). This shallow AML was also detected in the seismic data acquired in 1985 (Detrick et al., 1987; Kent et al., 1993b). The shallow AML at ~8°30′N was not previously imaged and extends for ~10 km (Figures 2a and S2).

North of the 9°03′N OSC the shallowest AML (~1450 m) is observed extending approximately from 9°40′ to 9°54′N, which encompasses the region where two documented eruptions occurred in 1991–92 and 2006 (e.g., Haymon et al., 1993; Soule et al., 2005; Tan et al., 2016; Figures 1b, 2b, and 4). From ~9°20′N to where the AML disappears at 10°06′N, AML depth variations are small (typically less than ~60 m). AML reflections detected south of 9°10′N along the eastern limb of the 9°03′N OSC are from a highly three-dimensional and discontinuous magma reservoir that is more accurately imaged in an earlier 3-D MCS study (Combier et al., 2008; Kent et al., 2000), and thus, these events are not discussed in detail here.

Significant variations in the strength of the AML reflection are observed over the survey area (Figure 2). The brightest AML reflection extends north of 9°38′N for about 60 km, encompassing the region of shallowest AML and continuing north to 10°06′N. Beneath the rest of the ridge axis, a weaker AML event is detected with local bright patches further south at around 8°30′N (for ~1 km where the AML is shallowest) and at 8°45′–48′N.

In Figure 2 the previously identified disruptions in the AML reflection event from Carbotte et al. (2013) are shown with minor modifications based on our 3-D swath results, where these disruptions can be identified with higher confidence (see next section). From the 2-D axial lines, AML disruptions are identified based on both reflection amplitude and traveltime characteristics and all meet at least two of the following criteria: break in AML continuity with abrupt step in twtt of $>$30 ms, gap in AML event of $>$400 m, edge diffraction in the stacked section indicating abrupt change in physical properties, abrupt change in AML amplitude, and/or presence of two AML events that overlap by $>$400 m. We note that the depth converted AML events (Figure 4) show more short-wavelength structure than the traveltime images, which is inherited in part from the two-layer constant-velocity assumption used for depth conversion. While our 2-D transects deviate significantly from the axial zone within the OSC region, the disruptions identified there are consistent with the 3-D seismic image of the AML of Combier et al. (2008). No identifications of AML disruptions are made in the regions of the southern segment where the 2-D seismic profile is not axially aligned.

As described in Carbotte et al. (2013), the majority of AML disruptions underlie or are located close to (within $\leq$1 km) seafloor discontinuities (24 out of 31, as indicated in Figures 2 and 4). Beneath some of the third-order discontinuities, most of which coincide with two overlapping axial summit troughs or pillow ridges with overlap lengths of 2–5 km, an AML segment spans some or all of the along-axis length of the offset zone on the seafloor (e.g., 9°56.2′–58.5′N; 9°18.4–20.9′N; 8°52.3–54.2′N). In Figure 6a the length distribution of individual AML segments defined by these disruptions is shown. Segments range in length from 3 to 15 km, cluster at 4–8 km with an average length of 6.5 km. Twenty-one segments are identified beneath the northern segment and 10 beneath the southern one. Due to significant axial misalignment of our 2-D profiles along the southern segment as well as lack of 3-D swath coverage, the identification of AML disruptions is more poorly constrained here. There are other additional possible disruptions that do not meet our minima criteria for identification (e.g., at 8°42′ and 8°47′N), and segmentation is likely underestimated in this region. The number of AML segments identified beneath each of the third-order structural segment varies from 2 to 6. The length distribution of the finest-scale seafloor structural segments, also shown in Figure 6a is close to that of the AML

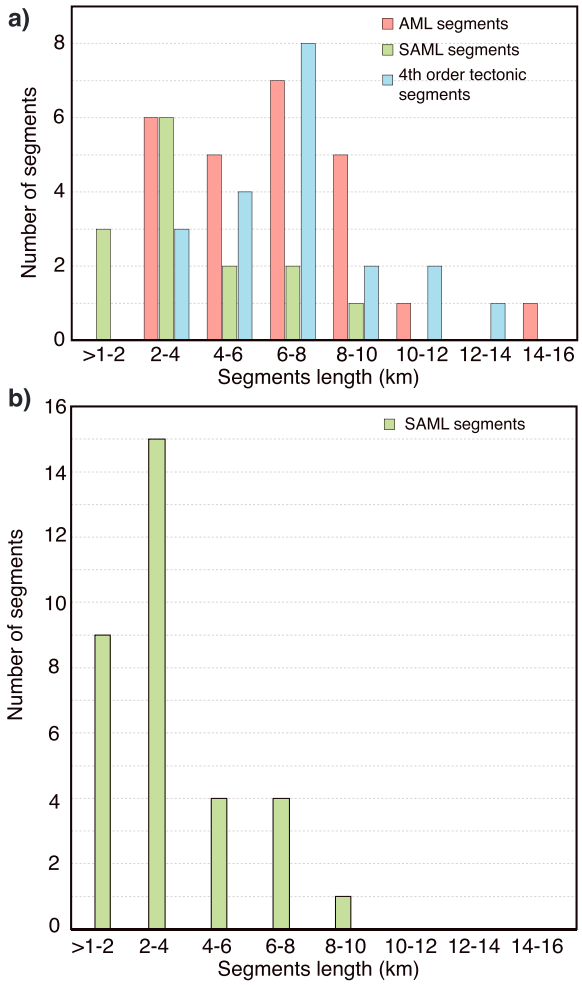

Figure 6. (a) Histogram comparing lengths of mapped axial magma lens (AML) segments, sub-AML (SAML) segments and fourth-order tectonic segments. SAML segments included in (a) are only the well-imaged and shallowest events north of 9°20′N (shown in blue in Figure 2). In (b) we show histogram of all mapped SAMLs. Structural segments are those shown in Figure 1 and included in Table 2 for the region of 3-D swath coverage.

segments, consistent with the finding that the AML disruptions and seafloor discontinuities that define this segmentation are well aligned. To provide some insight into the significance of the spatial correlations between the seafloor discontinuities and AML disruptions observed, we carried out a simple test comparing locations of seafloor discontinuities to a set of uniformly spaced (6 ± 1 km) AML disruptions. For six trials where the AML disruptions are offset by 1 km from one trial to the next, we find the uniformly distributed disruptions line up with on average, 37% of the fourth-order tectonic discontinuities. For comparison, the observations show that 77% of the AML disruptions lie within 1 km of a seafloor offset.

For the northern segment, excluding the OSC region (north of 9°12′N), a positive linear correlation between AML depth and depth of the seafloor is observed, whereas there is little correlation along the southern segment (Figure 5). To examine relationships with the third-order structural seafloor segments, the AML segments beneath each seafloor segment are identified (Table 2). For cases where the bounding seafloor discontinuity spans one or more identified AML segments, we include the AML segment closest in average twtt/depth to the neighboring AML segment beneath that structural segment. The one exception is the 9°37′N offset (seafloor expression extends to 9°38′N) where we interpret the boundary at the AML discontinuity at 9°39.9′N based on the larger step in AML twtt/depth at this location. Using these interpretations, weak to moderate correlations between AML and seafloor depth are observed for several of the third order segments (Figure 5), but with no consistent pattern. In a number of cases, average AML depths calculated for adjacent third-order segments show values that are close to or exceed the calculated standard deviations from the mean for those segments (e.g., along the northern segment; Table 2).

4.2.2. Three-Dimensional Swath—Across-Axis Structure

The 3-D swath data are used to examine the cross-axis characteristics of the AML disruptions and further refine their locations (Figures 3c and 3d, and 7). In most cases, the AML disruptions evident as gaps or small local deeps/steps in traveltime on the 2-D line coincide in the 3-D swath data with local deeps/steps that persist across the ~500-m width of the AML imaged. Except for the 9°37′N offset, all seafloor discontinuities in this region coincide with lateral offsets in the eruptive fissure zone of ~200 to <100 m and hence are much narrower than the disruption zone imaged in the AML below. The largest stepwise changes in AML depth are at 9°58.5′N (up to 40 m), 9°51.3′N (up to 40 m), 9°39.9′N (up to 60 m), and ~9°33.2′N (up to 60 m). Notably, some of the AML interruptions correspond with local deep zones that trend obliquely across the swath with respect to the ridge axis azimuth (Figure 7). For instance, the interruption identified at 9°44.7′N coincides in the 3-D swath data with a locally deeper AML that trends diagonally across the swath from 9°44′ to 9°45′N (Figures 3c and 3d, and 7c). Along this oblique zone, the 2-D axial line suggests that the northern AML lens plunges south beneath the southern one (Figure 2b). Similarly, the interruption at ~9°51.3′N corresponds with an oblique disruption zone, several kilometers long, with the southern shallower lens segment on-lapping the deeper, northern one (Figures 2b and 7a). This oblique-trending geometry is reminiscent of many seafloor discontinuities in the region where overlapping eruptive fissure zones or axial ridges are mapped (Escartín et al., 2007; Fornari et al., 1998; Soule et al., 2005; White et al., 2006). The 9°42.1′N and 9°47.9′N AML disruptions are more localized and represented by an abrupt change in AML traveltime; these disruptions are also more orthogonal to the axis trend (Figures 7b and 7d). Of the 14 AML disruptions identified using the 3-D swath data, 11 are located ≤1 km from a seafloor discontinuity.

Using the 3-D swath data, the interpretation of two AML disruptions are revised from the Carbotte et al. (2013) study. The discontinuity identified from a change in reflectivity in the 2-D axial line at 9°34.8′N is

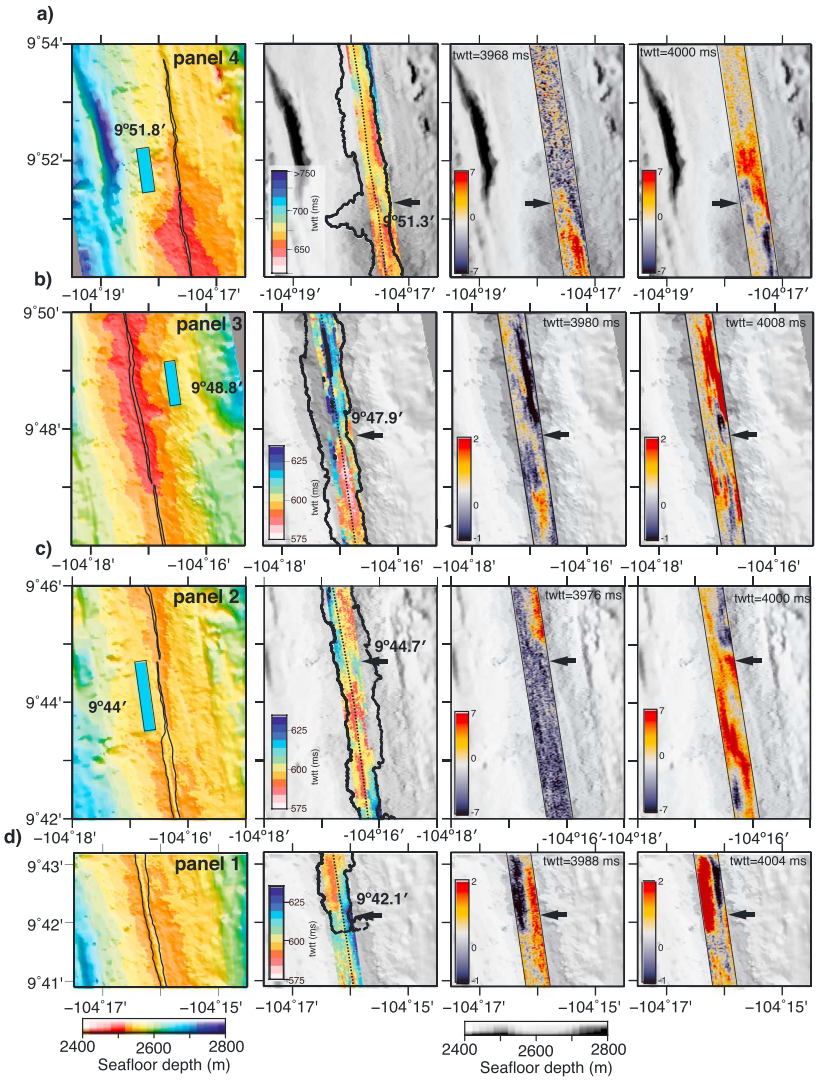

Figure 7. Plan view of the results obtained from 3-D swath data to illustrate travel time variations across four axial magma lens (AML) disruptions: (a) at 9°51.3′, (b) at 9°47.9′, (c) at 9°44.7′, and (d) at 9°42.1′N. For each AML disruption site, four panels are shown, from left to right: bathymetry map (White et al., 2006), AML picks from the swath data set as twtt below seafloor (Figure 3c), and two time slices of seismic amplitudes at selected twtt (indicated for each panel), superimposed on gray shaded bathymetry. Note the amplitude reversal across the identified AML disruptions indicating prominent steps in AML twtt. In bathymetry map, blue rectangles show location of the fourth-order tectonic discontinuities with the latitude indicated, and the black line outlines the axial summit trough (Escartín et al., 2007; Fornari et al., 1998; Soule et al., 2009). In addition to AML picks from the swath an outline of the AML mapped in 3-D cross-axis data set (Carton et al., 2010, 2014) is marked in black line. Location of the 2-D line, axis2r1, is shown in thin black dashed line. Black arrows denote approximate location of the AML disruption. Latitudinal extent of each panel is indicated in Figure 3c.

reinterpreted at 9°33.2′N where a stepwise change in reflector traveltime/depth is evident across the 3-D swath (Figure 3c). The disruption previously identified at 10°03.6′N is moved to 10°02.6′N where a change in the cross-axis dip of the AML is evident in the swath data coincident with a zone of reduced reflectivity in the 2-D axial line.

The average depth of the AML encompassed by the 3-D swath is 1,550 m, which is comparable to the average depth of the AML mapped from the 2-D line (1,560 m) within the same region (Figure 5, Table 2, and Appendix A). As observed along the 2-D axial line, significant differences are found in the average depth of the AML beneath the three adjacent third-order tectonic segments imaged, with minor variations in depth within each segment (Table 2).

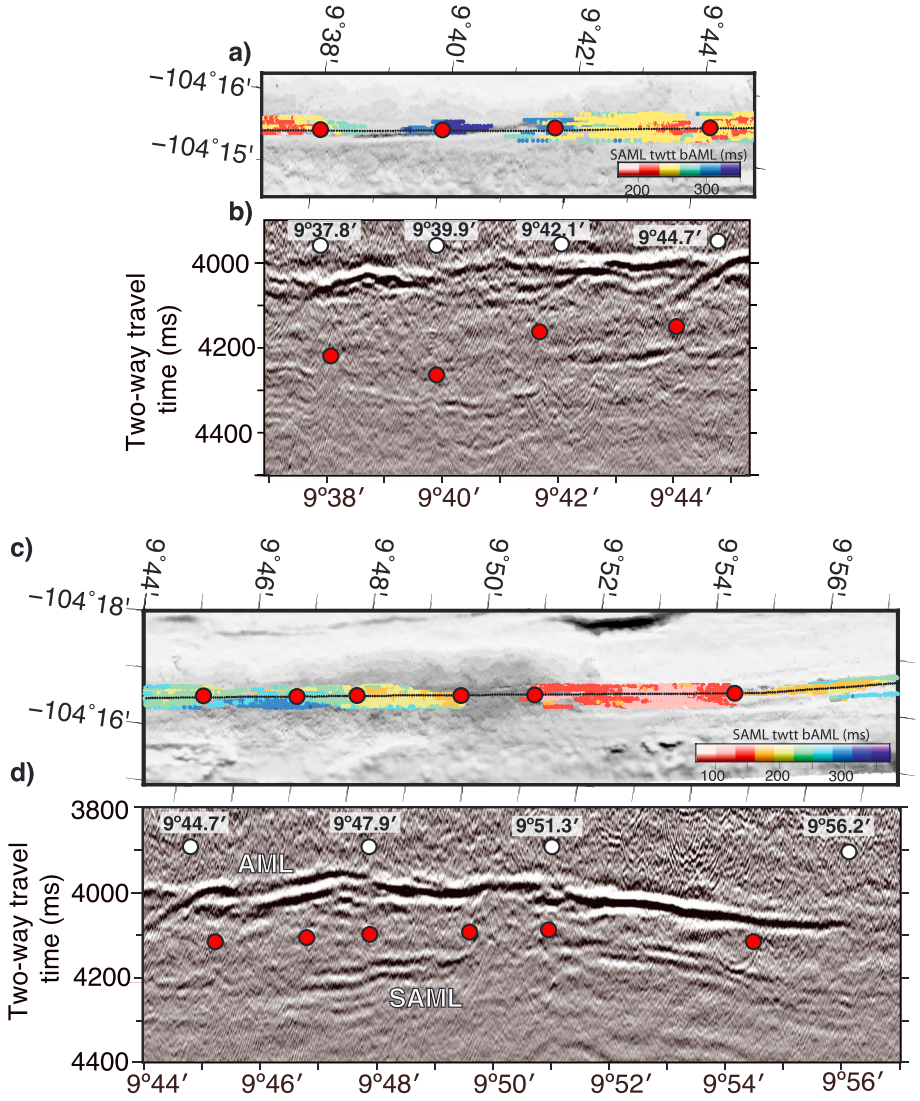

Figure 8. Comparison of subaxial magma lens (SAML) depth mapped from 3-D swath and from axis-centered 2-D seismic profile. (a, c) Plan view of SAML picks below axial magma lens (AML) from Figure 3f; (b, d) corresponding migrated seismic sections from profile axis2r1. Small disruptions in the shallowest SAML event including steps in travel time, gaps, and changes in reflector strength are identified and indicated with red circles. White circles in (b) and (d) indicate identified disruptions in AML. Thin dashed line in (a) and (c) indicates location of the corresponding section of profile axis2r1 shown in (b) and (d).

4.3. SAML Characteristics

4.3.1. Two-Dimensional Line—Axial Structure

Multiple levels of SAMLs are imaged intermittently along the EPR axis in our reflection data (Figures 2 and S1). The deepest SAMLs are detected up to 500-ms twtt (~1 km) below the AML but are weaker in amplitude, lower in frequency, and in general more discontinuous than the shallowest SAML and the AML above. The most abundant and brightest events are found north of 9°20′ extending to 10°01′ where the shallowest SAML reflections reside at depths of 100 to 800 m below the AML (Figures 2, 4, and 5). In this region, SAML reflections are present beneath most of the axis, but as observed for the AML, they are discontinuous with numerous small gaps and steps in reflector depth (Figures 2 and 8). Between these disruptions, SAML reflections indicate quasi-horizontal lens segments ranging from ~1 to 9 km in length along the axis (Figure 6). It is important to mention that although the velocity structure of zero-age crust beneath the AML is not well constrained, the abrupt lateral changes in velocities that would be needed to account for

the observed steps in SAML traveltimes are unlikely and we infer that the steps in SAML twtt are representative of true steps in SAML depth (~100 m on average).

Beneath the segment south of the 9°03′N OSC, SAMLs are sparser and where present, are shorter in length. Three vertically stacked SAMLs are found within the region from 8°48′-50′N; all are southward dipping and ≤3-km long (Figure 2a). A shorter <1-km SAML is identified beneath the shallow AML at 8°31′N. Elsewhere, weak possible SAML reflections that can be followed for only several hundreds of meters are found. Seafloor in this region is rougher than to the north (Figures 1 and S2), and noise from seafloor scattering obscuring the deeper section could in part account for the sparser SAML reflections detected.

Within the 9°03′N OSC region, an almost continuous ~4-km long SAML is observed beneath the eastern OSC ridge, extending between 9°05.5′ and 9°07.4′N (Figure S3). The same event is imaged in the ARAD 3-D MCS study, and its 3-D nature is examined and described by Arnulf et al. (2014).

In general, the strength of the SAML events and that of the AML reflector above are well correlated (Figures 2b and 8). For instance, within the area extending between 9°47′ and 9°54′N both SAMLs and AML are strong events; south of 9°29.6′N, a relatively weak SAML reflection underlies a weak AML. However, within some limited regions a relatively weak SAML is observed below a bright AML above (~9°42.1′–44.7′N), and vice versa (e.g., 9°20.9′–9°34.8′N).

4.3.2. Three-Dimensional Swath—Across-Axis Structure

The imaged SAMLs exhibit much lower amplitudes when compared to the SAMLs imaged in the composite 2-D line. This is likely a consequence of lower fold of the 3-D swath data, and hence lower signal-to-noise ratio. However, it is important to keep in mind that migration is performed differently (in 2-D versus in 3-D) for the two data sets (Figure A1; Appendix). As a result, there are places where SAMLs are not detected in the 3-D swath but are evident in the 2-D line (Figure 4).

Across the width of the 3-D swath, the SAMLs display somewhat larger variations in depth than observed along the ridge axis (Figure 5; 600 m total range compared with 500 m in 2-D line), which reflects minor cross-axis deepening of the SAML events (possibly due to undermigration). The stepwise changes in SAML depth and gaps in the reflection event observed in the axial line are also evident in many locations extending across the width of the 3-D swath (Figure 8). Notably, the SAML gap from 9°49′ to 51′N persists across the entire 3-D swath and has been attributed to melt draining associated with the 2006 eruption (Marjanović et al., 2014). As is also apparent in the 2-D axial line, many of the disruptions in the shallowest SAML coincide with or are located close to (within ~1 km) a disruption in the AML above (Figure 8). Notably, beneath several of the AML disruptions, the steps in the traveltime of the underlying SAML event are much larger than in the AML above. For instance, a traveltime step of >100 ms is observed in the SAML at 9°42.1′N, compared to <50 ms in the AML directly above it (Figure 8).

For the three third-order structural segments imaged within the area of the 3-D swath coverage, the SAML segments reside at a larger range of depths of 400–650 m compared with the AML above (150–250 m, Figure S4). Differences between average depths calculated for the adjacent third-order structural segments are similar for the SAML and the AML reflections (<100 m), but there is a much larger variance in SAML depths (standard deviations are 2–4 times larger, Table 2). Interestingly, deeper SAMLs reside beneath the central third-order segment, whereas the AML is shallowest in this region (Figures 5 and S4).

5. Discussion

In this section we discuss the implications of our study for factors that contribute to magma body depth, the significance of the distribution and characteristics of the SAML events for magmatic processes, and the relationship between the finest and intermediate-scale seafloor structural segmentation and structure of the underlying crustal magmatic system. To support this discussion, we include in Figure 9 a summary of results and interpretations from our study compared with axial properties derived from other studies of seafloor to uppermost mantle structure.

5.1. Controls on Axial Magma Lens Depth

The shallowest depths to which magmas can rise beneath mid-ocean ridges is believed to be governed primarily by a thermally controlled permeability barrier associated with the base of the dike section, linked to the balance between magma supply from the mantle and heat removal due to hydrothermal circulation

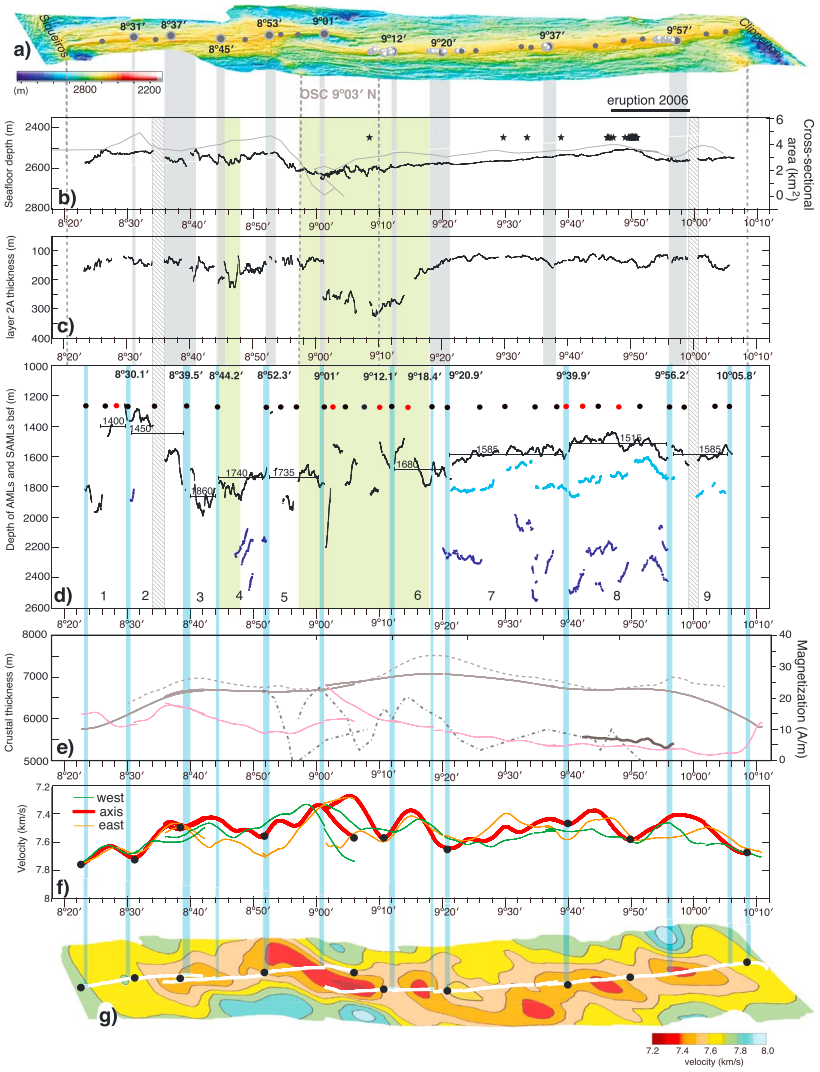

Figure 9. Summary of observations and interpretation of third-order tectonomagmatic segmentation along the EPR between the Siqueiros and Clipperton transform faults (TFs). (a) Seafloor bathymetry from Figure 1a. First- (Clipperton and Siqueiros TFs), second- (overlapping spreading center [OSC] 9°03′N), and third-order tectonic discontinuities are indicated in gray vertical bars with latitude labeled (projected to panels (b) and (c)). In addition in panel (a) locations of the third-order tectonic discontinuities are shown in gray circles and fourth-order tectonic offsets are marked by smaller gray dots. White-gray shaded circles indicate locations of axial pillow/lava domes from White et al. (2002). (b) Black line represents depth-converted, along-axis bathymetry profile from migrated seismic sections, as shown in Figure 4. Gray line shows ridge cross-sectional area from Scheirer and Macdonald (1993). Black stars indicate locations of vent sites (Von Damm, 2000; Fornari et al., 2012); they are shifted by ~100 m above the seafloor for visibility of the seafloor horizon. Black bar on top of the panel indicates the extent of the lava flow emplaced during the last documented eruption (from Soule et al., 2007). Gray hatched vertical bars indicate seismic data gap (low fold), and green shaded bars indicate regions where the seismic profiles were located >300 m from the axial zone. Dashed lines show location of the Clipperton and Siqueiros TFs and latitudinal extent of the OSC 9°03′N. (c) Along-axis layer 2A thickness from the 2-D axial lines. (d) Depth of the axial magma lens (AML; black) and sub-AML (SAML) reflectors (light blue—shallow and dark blue—deep/potential) below seafloor, mapped from 2-D lines (Figure 2). Blue vertical bars indicate the AML disruptions (latitude labeled) that we interpret as corresponding with the third-order tectonic discontinuities (projected to panels (e)–(g)). Horizontal bars show mean AML depth (mean value labeled) within the delimited segment. The locations of all identified AML disruptions are indicate with black/red dots plotted at ~1,250 m depth (black/red indicates those located ≤1 km/>1 km of a tectonic discontinuity, respectively). We note that the depth converted AML events show more short-wavelength structure than the travel time images, which is inherited in part from the two-layer constant velocity assumption used for depth conversion. (e) Compilation of inferred ridge axis crustal thicknesses from different studies is given in different styles of gray lines: Thick solid line indicates extrapolated crustal thickness extracted along the ridge axis from Canales et al. (2003); dashed line shows average crustal thickness within 25 × 20 km region around the ridge axis (as shown by Toomey & Hooft, 2008); dash-dotted line represents the extrapolated along axis crustal thickness extracted from Barth and Mutter (1996); and solid dark gray line indicates multichannel seismic (MCS)-derived crustal thickness for 10- to 50-kyr crust from Aghaei et al. (2014) for the 9°42′–9°57′N region (their Figure 12). Pink line represents crustal magnetization extracted along the ridge axis from Carbotte and Macdonald (1992). (f) Shallow mantle *P* wave velocity anomaly profiles along the ridge axis (thick red line), and 5 km away from the ridge axis on the eastern (thin orange line) and western (thin green line) flank. Profiles are extracted from the tomography model of Toomey et al. (2007, 2017); shown in map view in (g), black dots indicate local velocity highs defining extent of eight subcrustal magmatic segments for comparison with seafloor structural segmentation. Projected location of interpreted segment boundaries (black dots) are also shown in bottom panel. In bottom panel white lines indicate location of the ridge axis along which the 2-D profile is extracted. Note that panels (a) and (g) are rotated to add *depth* to the two dimensional illustration.

(Hooft et al., 1997; Natland & Dick, 2001; Phipps Morgan & Chen, 1993). From studies at both fast- and intermediate-spreading ridges, there is good evidence that regional-scale along-axis variations in mantle magma supply contribute to AML depth, with a shallower magma lens found in areas of higher supply as indicated by thicker crust (e.g., Baran et al., 2005; Canales et al., 2002; Carbotte et al., 2000), as predicted from numerical thermomechanical models (Phipps Morgan & Chen, 1993). However, superimposed on the large-scale variations are significant fluctuations in AML depth that occur over short spatial scales. From a study on the Southern EPR (SEPR) 16°–20°S, Hooft et al. (1997) hypothesized that local variations in magma withdrawal from the AML due to eruptions and hydrothermal cooling play the primary role in short wavelength variations in AML depth. These short-scale variations in AML depth may also reflect temporal changes in the position of the conductive thermal boundary layer separating the melt lens from the sheeted dike complex above it, which is inferred to vary by 200–400 m based on petrological observations at deep-sea crustal exposures and ophiolites (Gillis, 2008).

In our study, we find variations in AML depth of ~800 m, similar to the range found along the SEPR. Excellent constraints on the distribution of hydrothermal sites (Haymon et al., 1991, 1993; Von Damm, 1995; 2000; Fornari et al., 2012 and the references therein; Baker et al., 2016) are available for the northern segment of our study region where documented volcanic eruptions have also occurred providing the opportunity to further explore the impact of these heat removal processes. Our results show that the AML is locally shallowest and brightest in the region of recent documented volcanic eruptions from 9°46′–56′N (Soule et al., 2007; Tan et al., 2016) where the most abundant and sustained hydrothermal venting is also found (Von Damm, 2000; Fornari et al., 2012), and hence where heat extraction from both processes is expected to be the highest (Figure 1b, 2b, 4, and 9). The most abundant SAMLs are found in this region (Figure 2b) indicating that more melt is present below the AML in the middle crust.

This region is also the site of the shallowest axial depths for the entire northern segment (Figures 4 and 9b), larger cross-sectional area (Figure 9b, Scheirer & Macdonald, 1993), and low residual gravity anomalies (Wang et al., 1996) indicative of lower axial densities. Crustal thickness, which is a measure of time-integrated magma supply, is similar to elsewhere along the ridge and there is no evidence for longer-term higher magma supply from the mantle in the region (Figure 9e) (Aghaei et al., 2014; Canales et al., 2003). We speculate that the warmer axial thermal structure inferred from the shallow AML and more abundant melt in the crust in this region reflects higher rates of magma delivery to the crust at present. Enhanced magma delivery in the ~9°50′N region likely reflects the influence of the mantle source for the nearby Lamont seamounts, which is a prominent near-axis seamount chain located on the west flank of the ridge (e.g., Fornari et al., 1988). Interestingly, there is also evidence for anomalous near-axis melt sources to the east in this region, with prominent off-axis magma lenses (OAML) in the crust located up to 8 km east of the ridge axis (Canales et al., 2012) and the near-axis Watchstander seamount chain found further to the north (Macdonald et al., 1992).

The region of shallowest AML along the ridge south of the 9°03′N OSC is located at 8°30′N and is also a region of shallow axial depths (~2525 m) and broad axial high (Figure 9b), where a nearby off-axis volcanic ridge is present indicative of a local near-axis melt anomaly (Figures 1 and S2). The 8°30′N site represents one of the few regions along the southern segment along which a seismic reflection signal from SAMLs is identified (Figure 2a). In addition, an earthquake swarm was recorded in 2001 just north of this region (Figure S2), between 8°37′ and 42′N, and was most probably triggered by magmatic activity in the area with hydrothermal signals also detected around 8°37′–38′N (Bohnenstiehl et al., 2003). By analogy with the well-studied 9°50′N eruption site, these characteristics suggest that the 8°30′N area might also be an area of active volcanism and enhanced magmatic activity. Similar to 9°50′N, the crust is not significantly thicker in this region (Canales et al., 2003; Figure 9e) and more frequent mantle melt injection at present may account for the shallow melt/warmer upper crustal temperatures inferred here.

5.2. Implications of SAML Characteristics for Crustal Magmatic Processes

Key findings of our study pertain to the geometry and depth of the SAMLs and include the observations that these melt bodies: (1) form quasi-horizontal lens segments similar to the AML segments (Figures 2, 6, and 8), (2) are more variable in depth over short spatial scales than the AML (Figures 5 and S4 and Table 2), and (3) disruptions in both the SAML and AML are vertically aligned in some locations indicating coincident segmentation. With magma present in the crust beneath most of the EPR in our study region, an important question is to understand why does melt segregate into a series of short lens segments rather than form a continuous

melt reservoir (Carbotte et al., 2013). Hydrothermal convection in the upper crust may play an important role with local deepening and a more crystalline magma lens predicted at sites of fluid downflow in models of hydrothermal flow (Fontaine et al., 2011). Support for this model is provided by a recent study of the high-resolution velocity structure (Marjanović et al., 2017) and local microseismicity study (Tolstoy et al., 2008) studies, both focused on the 9°50′N region. The former study infers presence of fluid down-flow zones associated with the change in width of the AST at 9°44′N and 9°51.8′N, which are directly underlain by AML disruptions (Figures 2b, 4, 7). In addition, both studies show focused fluid down-flow coincident with the small jog in the AST at ~9°48.8′N. However, the nearest disruption in the AML is located ~2 km to the south at 9°47.9′ and not directly beneath the inferred hydrothermal down-flow zone.

Alternatively, deeper processes such as formation of melt channels in the lower crust, the presence of local sites of dike intrusion from the mantle, or along-axis convection within the melt-rich mush zone of the lower crust may also give rise to segmentation of the shallow melt reservoir (Fontaine et al., 2017; Kelemen et al., 1995; Natland & Dick, 2001; Sinton et al., 1991). While a closely coupling of hydrothermal and magmatic systems is expected our observations of the SAML geometry supports the hypothesis that patterns of melt transport in the lower crust, rather than shallow upper crustal processes, play the dominant role in magma reservoir segmentation. First, it is difficult to envision how the thermal effects of hydrothermal circulation cells in the dike section could propagate below the AML and lead to segregation of deeper melts into quasi-horizontal lenses that are more variable in depth than the AML above. Furthermore, a weak negative correlation is found between SAML depth and AML depth (Figure S4), such that where the AML (and seafloor) is shallower, the SAML tend to be deeper not shallower, contrary to predictions if the depths of these features were governed by the shallow thermal regime.

Our preferred interpretation is that the SAMLs reflect instability zones, likely to be short lived, that form and ascend through the melt-crystal mush of the lower and middle crust. Such instability zones may develop owing to, for example, buoyancy driven overpressurization, compositional barriers, rheological contrasts, or as melt compaction waves (e.g., Gudmundsson, 1990, 2011; Menand, 2008, 2011; Miller et al., 2011; Parsons et al., 1992; Phipps Morgan & Chen, 1993; Rabinowicz et al., 2001; Taisne & Jaupart, 2009), all closely linked to the local history of magma replenishment and transport through the crust. The observation that the AML varies less in depth than the SAMLs found beneath it may reflect the important role that the base of the dike section plays as a permeability boundary that impedes upward melt migration at the shallowest crustal levels. The along-axis lengths of the imaged SAML segments are somewhat shorter than that of the AML segments above (Figure 6a), which likely, in part, reflects imaging limitations due to greater attenuation of seismic energy in the hot melt-rich crust beneath the AML. However, it is possible that the difference in length distributions also reflects the aggregation and coalescence of these melt instability zones as they ascend to the base of the dike section.

Similar factors may also explain the characteristics of OAMLs found in our study area (Han et al., 2014). While the shallowest (and largest) OAMLs pond at similar depths consistent with the base of the dike section formed at the ridge axis, the smaller and deeper ones are found at a wider range of depths that, depending on thermal model assumed and inferred crustal age, correspond with the ductile-brittle transition (Canales et al., 2012; Han et al., 2014) and hence may be rheologically controlled (Menand, 2011). Additional evidence for deep sills at MOR comes from seismic imaging of a large number of subhorizontal magmatic sills stacked one on top of the other in the uppermost mantle beneath the ultramafic Rainbow massif, along the Mid-Atlantic Ridge (Canales et al., 2017). The length of these sills ranges from 0.2 to 1.2 km. Similarly to the EPR, the depth of the shallowest sills seem to coincide with a rheological boundary inferred from the presence of sharp velocity contrast between the less altered, high-velocity core of the massif and highly serpentinized, low-velocity overlying layers; the deeper sills seem to be rather randomly distributed spanning depths of ~8 km.

5.3. Relationship Between Seafloor Structural Segmentation, crustal Magma Lenses and Uppermost Mantle Melt Distribution

5.3.1. Third- and Fourth-Order Segmentation

Recent observations from the EPR suggest that the larger third-order scale of structural segmentation of the ridge axis reflects coherent volcano-magmatic units extending from the seafloor into the uppermost mantle (White et al., 2000, 2002; Haymon & White, 2004; Toomey et al., 2007). From their analysis of near-bottom

sonar and photo studies of volcanic structures and lava flow morphology from 9°09′ to 9°54′N and along the SEPR from 17°11′ to 18°37′S, White et al. (2000, 2002) find that lava domes and pillow lava flows are concentrated at the ends of the third-order segments indicating decreased eruption effusion rates and increased lava viscosity (Figure 9a). In comparison, higher effusion-rate sheet flows are found within segment centers along with more abundant hydrothermal vents and biological communities, suggesting magmatic heat sources are focused near the center of third-order segments (Haymon & White, 2004). Based on these observations White et al. (2000, 2002) propose that third-order segments represent coherent volcano-magmatic units, each with a common crustal-level volcanic plumbing system.

Our study encompasses nine third-order structural segments and provides the opportunity to examine the relationships with magma distribution in the crust as well as melt distribution in the uppermost mantle imaged in the seismic tomography study of Toomey et al. (2007). Both of these seismic studies provide snapshots of the modern-day magma distribution, with the subcrustal mantle melt zone the source reservoir for the crustal magmatic system. The crustal observations presented here indicate segmentation of the AML that is closely coupled with the finest-scale segmentation of the axial eruptive fissure zone, consistent with previous inferences (Carbotte et al., 2013). North of 9°20′N where the AML segmentation is well constrained by the 3-D swath data, 80% (11/14) of AML disruptions are located within 1 km of a discontinuity identified in the seafloor above. Further, the swath data show that AML disruptions correspond with local deeps of diminished reflectivity that extend across the ~500-m imaged width of the AML, in contrast to the narrower $<$200 m wide offset zone at the seafloor.

Comparison of AML and layer 2A properties with the third-order seafloor segmentation suggests an organization of the crustal magmatic system on these longer length scales as well. In Figure 9, we present our interpretation of the relationships between the third-order seafloor segments and the underlying magmatic system. We find that locations of the third-order seafloor discontinuities are well aligned in many locations with changes in layer 2A structure as well as with disruptions in the AML and SAMLs below. Furthermore, in some cases the groups of AML segments that underlie third-order structural segments reside at similar depths, suggestive of a similar magmatic heat flux along these structural units (e.g., segments 7–9; Figures 5 and 9 and Table 2). In addition, individual third-order segments are characterized by a relatively uniform layer 2A thickness with small but significant differences (10%–15% as measured from the 3-D swath data) from one third-order segment to the next suggesting they represent independent units in their longer-term volcanic eruption history. Comparison with the subcrustal melt distribution of Toomey et al. (2007) shows that for many (although not all) third-order seafloor offsets, there is a good vertical alignment with the higher velocity/lower melt edges of the punctuated subcrustal melt zones imaged in that study and with disruptions in the AML and SAML in the crust (Figures 9f and 9g). The punctuated melt zones also show a variable degree of axial alignment with several melt centers laterally offset from the axis, most notably beneath the third-order structural segment from 9°20′ to 37′N. Comparisons of AML depth with the alignment of subcrustal melt shows a general relationship of deeper AML where the subcrustal melt distribution is not axially centere+aterally smooth seismic velocity models along transects through 150 and 300 kyr crust. The results indicate a relatively uniform crustal thickness from Clipperton to Siqueiros except for the local zone of anomalously thicker crust just north of the OSC (Figure 9e). The MCS derived crustal thickness estimates of Barth and Mutter (1996) obtained for crustal ages of ~35–500 kyr and are suggestive that intermediate-wavelength variations may be present (Figure 9e). However, spatial resolution is also poor for this data set with only 15 cross-axis lines spaced 5–10 km apart extending from 8°50′ to 9°50′N. The two data sets forming the basis of the Canales et al. (2003) and Barth and Mutter (1996) studies are thus inadequate to evaluate relationships with the current axial magma distribution. More recently, Moho was identified in crust as young as 10 kyr up to crustal ages of 180 kyr in the high-resolution 3-D MCS study of Aghaei et al. (2014) for the 9°42–57′N region and in this data set, coherent spatial variations consistent with the modern magmatic segmentation are observed, including in the inferred thickness of the Moho transition zone as well as in crustal thickness estimates. Similar data over larger areas will be needed to further explore these relationships.

5.3.2. Large Second-Order Scale Segmentation

There is some indication in our data for coherent differences between the larger-scale ridge segments north and south of the 9°03′N OSC. Average properties differ for the two segments with a number of characteristics indicating more restricted magma delivery at present to the southern segment, except locally at 8°30′N. These include AML reflections that are weaker and deeper on average suggestive of a cooler crustal

regime, as well as presence of only weak and sparse SAML events (Figures 2, 5, and 9). Layer 2A is more variable and thicker on average, consistent with the presence of a deeper AML along this segment as predicted by the Buck et al. (1997) model of extrusive layer accumulation.

Deeper processes may also contribute. A regional-scale geochemical study of seafloor lava compositions along the northern EPR indicate differences in the mantle melt source for the two segments with higher Sr isotopic compositions and Ba/Ti ratios measured from the southern segment indicative of a more enriched mantle source, (Langmuir et al., 1986). Analysis of magnetic anomaly data in the region shows higher magnetizations associated with the southern segment at present and throughout the Brunhes period (past 0.78 Myr) indicating the presence of more Fe-rich crustal rocks (Carbotte & Macdonald, 1992; Figure 9e). Furthermore, spreading rates for the two segments estimated from magnetic reversals differ over the past 1 Myr with a significant spreading rate asymmetry (22% faster to the west) and faster spreading (by 8%) averaged over the Brunhes at the southern segment, indicating that these segments have persisted as distinct tectono-magmatic units for at least this time period.

Building from the observations of Toomey et al. (2007) as well as from new observations of upper mantle structure beneath the Endeavor segment, VanderBeek et al. (2016) propose that misalignment of mantle flow relative to the ridge axis contributes to plate boundary reorganization that is accommodated by the formation and propagation of second-order tectonic offsets including the 9°03′N OSC at the northern EPR. The recent history of the 9°03′N OSC is well documented from magnetic anomaly data which shows that this offset evolved from a smaller preexisting offset in response to a counterclockwise change in plate motion since 1 Ma (Carbotte & Macdonald, 1992). We infer that the preexisting small offset was inherited from ~25-km scale punctuated melt reservoirs below the base of the crust like those beneath the ridge axis at present. Why this particular offset, out of the many that presumably existed along the axis at the time, began to lengthen and propagate in response to plate motion change is an important question. That the larger-scale segments bounded by the 9°03′N OSC at present exhibit distinct segment-scale properties and longer-term spreading history suggests that differences in the underlying mantle melt sources may have contributed to maintain these segments as distinct tectono-magmatic units for long time periods through this period of plate boundary reorganization.

6. Summary and Conclusions

In this study, 2-D and 3-D swath MCS data are used to characterize the shallow portion of the crustal magmatic system beneath the EPR from 8°20′N to 10°10′N with implications for magmatic segmentation and melt transport in the crust. Primary findings and conclusions include the following:

1. The two regions of shallowest AML in our study area are located from 9°40′ to 56′N, where recent volcanic eruptions are documented, and from 8°29′ to 34′N beneath a region that is morphologically similar to the 9°50′N eruption site, and which may also be volcanically active. Near-axis seamount chains and ridges are found in both regions and the presence of anomalous mantle melt sources associated with this ridge flank volcanism may contribute to enhanced melt in the crust at present in both locations. Over larger length scales, a number of characteristics suggest that the ridge axis south of the 9°03′N OSC has a more restricted magma budget at present except locally at 8°30′N. AML depths averaged for the region are deeper, layer 2A is more variable and thicker on average, and AML reflections are typically weaker and SAMLs are sparse.
2. The 3-D along-axis swath data are used to further refine the location of previously identified AML disruptions and to define the cross-axis characteristics of the fine-scale AML segmentation. The data show that AML disruptions identified from local lows or stepwise changes in AML depth directly beneath the axial eruption zone are present across the full width of the AML imaged in the 500- to 800-m-wide swath and are often oblique trending relative the ridge axis orientation. The length distribution of the AML segments matches well with that of the fine-scale structural segmentation with the average length of AML and structural segments of 6.5 and 7 km, respectively, consistent with prior interpretations of closely coupled fine-scale tectonomagmatic segmentation.
3. SAMLs are imaged along the ridge axis at multiple levels with the brightest and most widespread SAML reflections found north of 9°20′N. The SAMLs are segmented similar to the AML above them into quasi-horizontal lens segments 1- to 9-km long bounded by disruptions that are often marked by stepwise

changes in reflection traveltime/depth. The shallowest SAML segments are located from 100 to 800 m beneath the AML and are more variable in depth than the AML. From these characteristics we infer that the SAMLs are short-lived instability zones that ascend through the crust and can reside at a wider range of depths than the shallowest melt reservoir, the AML, the depth of which is constrained by the permeability/strength boundary at the base of the dike section.

4. The combined 2-D/3-D swath MCS data set is used to characterize properties of the imaged magma lenses and layer 2A beneath nine third-order structural segments identified in this region. In many cases the two to six AML segments that underlie these seafloor segments reside at similar average depths and we infer that they share a common longer-term magmatic source. Further, the 3-D swath data show that average layer 2A thickness varies by ~10%–15% from one third-order segment to the next indicating that the time-averaged volcanic constructional and hydrothermal processes that control the thickness of this layer also vary on these length scales. Previously imaged discrete low-velocity zones within the shallow mantle roughly coincide with these structural segments. Collectively, the observations support the hypothesis that third-order structural segments reflect coherent volcano-magmatic units extending from the seafloor into the uppermost mantle. The ~6-km finer-scale segmentation of melt lenses in the shallow crust may reflect the distribution of lower crustal melt channels or injection sites fed from the larger subcrustal mantle melt reservoirs.

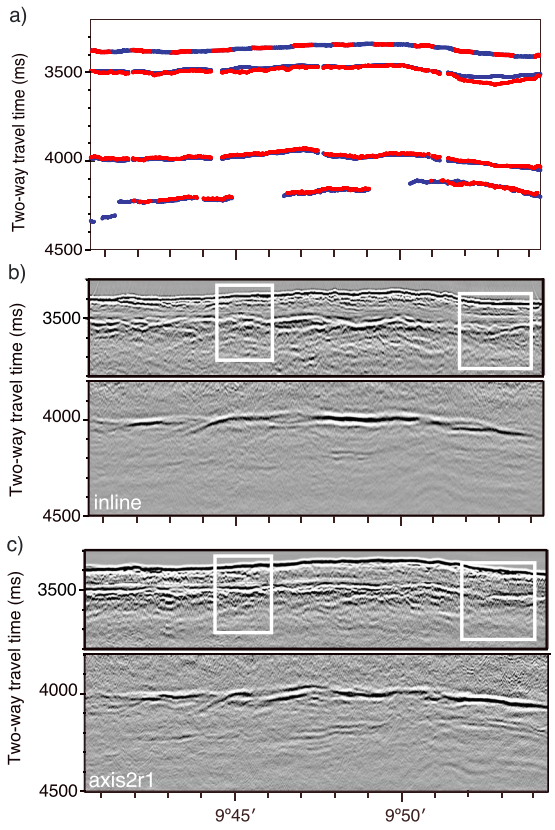

Figure A1. (a) Comparison between horizons picks (seafloor, layer 2A, AML, and shallowest SAML) extracted from 2-D processed line (blue) and coincident picks extracted from the along-axis 3-D swath (red) for the region of the 2006 eruption delimited in Figure 3a. (b) Seismic section is an in-line extracted from the along-axis 3-D swath, to approximately match the location of the 2-D line (axis2r1) for the region between ~9°41′ and 9°54′N. (c) Migrated 2-D seismic line (axis2r1) for the same region as the inline shown in (b). Regions of discrepancies in layer 2A picks are marked in white rectangles (see appendix text). The seismic sections in (b) and (c) are separated into two panels with different gains applied in order to best display the layer 2A, and AML/SAML events. AML = axial magma lens; SAML = sub-AML.

Appendix A: Comparison of 2-D line and 3-D Swath Data for Imaging Crustal Properties Within the Innermost Axial Zone

To accurately image and resolve the true dips and locations of geological structures within the subsurface, three-dimensional surveys are required. However, due to the high cost of acquisition, only a handful of 3-D MCS experiments have been conducted with the focus on MORs (e.g., Aghaei et al., 2017; Kent et al., 2000; Momoh et al., 2017; Singh et al., 2006). Instead, along axis 2-D profiling has been commonly used to examine properties of zero-age oceanic crust, including imaging of the AML (e.g., Babcock et al., 1998; Baran et al., 2005; Carbotte et al., 1997, 2000, 2008; Detrick et al., 1987; Hooft et al., 1997; Kent et al., 1993a, 1993b, 1994; Mutter et al., 1988, 1995).

Here we compare imaging results using the along-axis 3-D swath and the 2-D axially centered line for crustal properties within the innermost axial zone along an ~70-km long stretch of the EPR segment north of 9°20′N. For each horizon mapped within the 3-D swath (Figure 3) we extract picks coincident with those from the 2-D line (Figure 2b) and compare the two (Figure A1a). For most of the examined profile extending between ~9°40′ and 9°55′N, the match between the coincident picks for the identified horizons is within the picking error. However, at ~9°45′N and 9°53′N we observe local discrepancies in the layer 2A event, resulting in up to 60-m thicker layer 2A in the 3-D swath over distance 1.5 to 3 km (Figure A1a). Comparison of the seismic images indicates local complexities in layer 2A in these regions, possibly originating from different generations of lava flows, that are not well-imaged in the composite, 2-D migrated line. For instance, at 9°45′N while the layer 2A horizon is evident as a single event in the 2-D profile, in the 3-D swath three interlaced events are present with the deeper event slightly stronger in amplitude and hence captured in the automated picking of this horizon (Figures A1b and A1c). Similar observations are found for the discrepancy observed north of 9°53′N. It is noteworthy that the amplitudes of the AML and SAML events appear stronger and in places more continuous in the 2-D profile. This reflects the higher fold of the 2-D processed data, which is constructed as a composite line using two streamers and hence exhibits

higher signal to noise ratio than a single inline from the 3-D swath. From this comparison, we infer that for mapping properties of deeper events (AML and SAMLs) beneath the axial zone, the 2-D line geometry may be adequate. However, for the layer 2A event, which varies significantly in cross-axis direction, the 3-D swath geometry provides improved imaging of axial zone properties. By comparing average values for fine-scale segments (Table 2), we observe differences, which are due to the lateral variations within the zone encompassed by the 800-m-wide swath.

For properly mapping lateral variations and collapsing diffracted energy accurately, the width of the along-axis swath available for 3-D migration must be greater than was available for our study, that is, adequate migration aperture must be taken into account. For instance, for the average depth of the AML in our region the first Fresnel zone that captures 70% of the diffracted energy (Cordsen et al., 2000) is ~500-m wide, which means that for imaging the AML in 3-D the along-axis swath should be at least 500-m wider than the width of the AML; to capture 95% of diffracted energy and image properly the AML, assuming 30° scattering angle (Xde = $Z_{AML} \times \tan 30°$, where Xde is the width of the zone and Z_{AML} is the depth of the AML below sea surface), the along-axis swath should be ~2.5-km wider than the AML (1.25 km on each side).

Acknowledgments
We thank the crew of the MGL0812 expedition aboard R/V Marcus G. Langseth. Special thanks to the Captain M. Landow and technical staff led by R. Steinhaus and Science Officer A. Johnson for their efforts that led to a successful research cruise. We are grateful to D. J. Fornari, D.R. Toomey, and an anonymous reviewer for their comments and suggestions that significantly improved the manuscript. Seismic data from this study are archived with the IEDA MGDS (Mutter et al., 2008) and Academic Suport Portal (ASP) at UTIG (Marjanović et al., 2018). We would also like to thank Vicki Ferrini for Matlab code for manipulating data grids. Software packages *Focus* and *VoxelGeo* by Paradigm Geophysical were used for seismic data processing and interpretation. This research was supported by NSF awards OCE0327872 to J. C. M. and S. M. C., OCE-0327885 to J. P. C., and OCE0624401 to M. R. N.

References

Aghaei, O., Nedimović, M. R., Carton, H., Carbotte, S. M., Canales, J. P., & Mutter, J. C. (2014). Crustal thickness and Moho character of the fast-spreading East Pacific Rise from 9°42′N to 9°57′N from poststack-migrated 3D MCS data. *Geochemistry, Geophysics, Geosystems*, *15*, 634–657. https://doi.org/10.1002/2013GC005069

Aghaei, O., Nedimović, M. R., Marjanović, M., Carbotte, S. M., Pablo Canales, J., Carton, H., & Nikić, N. (2017). Constraints on melt content of off-axis magma lenses at the East Pacific Rise from analysis of 3-D seismic amplitude variation with angle of incidence. *Journal of Geophysical Research: Solid Earth*, *122*, 4123–4142. https://doi.org/10.1002/2016JB013785

Arnulf, A. F., Singh, S. C., & Pye, J. W. (2014). Seismic evidence of a complex multi-lens melt reservoir beneath the 9°N Overlapping Spreading Center at the East Pacific Rise. *Geophysical Research Letters*, *41*, 6109–6115. https://doi.org/10.1002/2014GL060859

Babcock, J. M., Harding, A. J., Kent, G. M., & Orcutt, J. A. (1998). An examination of along-axis variation of magma chamber width and crustal structure on the East Pacific Rise between 13°30′N and 12°20′N. *Journal of Geophysical Research*, *103*(B12), 30,451–30,467. https://doi.org/10.1029/98JB01979

Baker, E. T., Resing, J. A., Haymon, R. M., Tunnicliffe, V., Lavelle, J. W., Martinez, F., et al. (2016). How many vent fields? New estimates of vent field populations on ocean ridges from precise mapping of hydrothermal discharge locations. *Earth and Planetary Science Letters*, *449*, 186–196.

Baran, J. M., Cochran, J. R., Carbotte, S. M., & Nedimović, M. R. (2005). Variations in upper crustal structure due to variable mantle temperature along the Southeast Indian Ridge. *Geochemistry, Geophysics, Geosystems*, *6*, Q11002. https://doi.org/10.1029/2005GC000943

Barth, G. A., & Mutter, J. C. (1996). Variability in oceanic crustal thickness and structure: Multichannel seismic reflection results from the northern East Pacific Rise. *Journal of Geophysical Research*, *101*(B8), 17,951–17,975. https://doi.org/10.1029/96JB00814

Bohnenstiehl, D. R., Tolstoy, M., Fox, C. G., Dziak, R. P., Chapp, E., Fowler, M., Haxel, J. (2003). Anomalous seismic activity at 8°37-42′N on the East Pacific Rise, *Ridge 2000* Events, 18-20.

Buck, W. R., Carbotte, S., & Mutter, C. Z. (1997). Controls on extrusion at mid-ocean ridges. *Geology*, *25*(10), 935–938. https://doi.org/10.1130/0091-7613(1997)025<0935:COEAMO>2.3.CO;2

Canales, J. P., Carton, H., Carbotte, S. M., Mutter, J. C., Nedimović, M. R., Xu, M., et al. (2012). Network of off-axis melt bodies at the East Pacific Rise. *Nature Geoscience*, *5*(4), 279–283. https://doi.org/10.1038/ngeo1377

Canales, J. P., Detrick, R. S., Toomey, D. R., & Wilcock, W. S. D. (2003). Segment scale variations in the crustal structure of150–300 kyr old fast spreading oceanic crust (East Pacific Rise, 8°15′N–10°15′N) from wide-angle seismic refraction profiles. *Geophysical Journal International*, *152*(3), 766–794. https://doi.org/10.1046/j.1365-246X.2003.01885.x

Canales, J. P., Dunn, R. A., Arai, R., & Sohn, R. A. (2017). Seismic imaging of magma sills beneath an ultramafic-hosted hydrothermal system. *Geology*, *45*(5), 451–454. https://doi.org/10.1130/G38795.1

Canales, J. P., Ito, G., Detrick, R. S., & Sinton, J. (2002). Crustal thickness along the western Galapagos Spreading Center and the compensation of the Galapagos hotspot swell. *Earth and Planetary Science Letters*, *203*(1), 311–327. https://doi.org/10.1016/S0012-821X(02)00843-9

Carbotte, S., & Macdonald, K. (1992). East Pacific Rise 8°–10°30′N: Evolution of ridge segments and discontinuities from SeaMARC II and three-dimensional magnetic studies. *Journal of Geophysical Research*, *97*(B5), 6959–6982. https://doi.org/10.1029/91JB03065

Carbotte, S. M., Canales, J. P., Nedimović, M. R., Carton, H., & Mutter, J. C. (2012). Insights into mid-ocean ridge hydrothermal and magmatic processes from recent seismic studies at the EPR 8°20′–10°10′N and Endeavour Segments. *Oceanography*, *25*(1), 100–112.

Carbotte, S. M., Marjanović, M., Carton, H. D., Mutter, J. C., Canales, J. P., Nedimović, M. R., et al. (2013). Fine-scale segmentation of the crustal magma reservoir beneath the East Pacific Rise. *Nature Geoscience*, *6*(10), 866–870. https://doi.org/10.1038/ngeo1933

Carbotte, S. M., Mutter, J. C., & Xu, L. (1997). Contribution of tectonism and volcanism to axial and flank morphology of the southern EPR from a study of Layer 2A geometry. *Journal of Geophysical Research*, *102*(B5), 10,165–10,184. https://doi.org/10.1029/96JB03910

Carbotte, S. M., Nedimović, M. R., Canales, J. P., Kent, G. M., Harding, A. J., & Marjanović, M. (2008). Variable crustal structure along the Juan de Fuca Ridge: Influence of on-axis hot spots and absolute plate motions. *Geochemistry, Geophysics, Geosystems*, *9*, Q08001. https://doi.org/10.1029/2007GC001922

Carbotte, S. M., Ponce-Correa, G., & Solomon, A. (2000). Evaluation of morphological indicators of magma supply and segmentation from a seismic reflection study of the EPR 15°30′–17°N. *Journal of Geophysical Research*, *105*(B2), 2737–2759. https://doi.org/10.1029/1999JB900245

Carbotte, S. M., Small, C., & Donnelly, K. (2004). The influence of ridge migration on the magmatic segmentation of mid-ocean ridges. *Nature*, *429*(6993), 743–746. https://doi.org/10.1038/nature02652

Carbotte, S. M., Smith, D. K., Cannat, M., & Klein, E. M. (2015). Tectonic and magmatic segmentation of the Global Ocean Ridge System: A synthesis of observations. In T. J. Wright, A. Ayele, D. J. Ferguson, T. Kidane, & C. Vye-Brown (Eds.), *Magmatic rifting and active volcanism, Special Publications* (Vol. 420, pp. 249–295). London: Geological Society. https://doi.org/10.1144/SP420.5

Carton, H.D., Carbotte, S.M., Mutter, J.C., Canales, J.P., and Nedimović, M.R. (2014). Axial magma system geometry beneath a fast-spreading mid-ocean ridge: Insight from three dimensional seismic reflection imaging on the East Pacific Rise 9°42 to 9°57′N, Abstract V22A- 91502, *Presented at 2014 Fall Meeting,* AGU, San Francisco, Calif., 15–19 Dec.

Carton, H. D., Carbotte, S. M., Mutter, J. C., Canales, J. P., Nedimović, M. R., Aghaei, O., et al. (2010). Three-dimensional seismic reflection images of axial melt lens and seismic layer 2A between 9°42′N and 9°57′N on the East Pacific Rise, Abstract OS21C-1514, *Presented at 2010 Fall Meeting*, AGU, San Francisco, California.

Collier, J. S., & Singh, S. C. (1997). Detailed structure of the top of the melt body beneath the East Pacific Rise at 9°40′N from waveform inversion of seismic reflection data. *Journal of Geophysical Research*, *102*(B9), 20,287–20,304. https://doi.org/10.1029/97JB01514

Combier, V., Singh, S. C., Cannat, M., & Escartin, J. (2008). Mechanical decoupling and thermal structure at the East Pacific Rise axis 9°03′N: Constraints from axial magma chamber geometry and seafloor structures. *Earth and Planetary Science Letters*, *272*(1-2), 19–28. https://doi.org/10.1016/j.epsl.2008.03.046

Cordsen, A., Galbraith, M., & Peirce, J. (2000). *Planning land 3D seismic surveys*, *Geophysical Developments Series No 9*. Tulsa: Society of Exploration Geophysicists. https://doi.org/10.1190/1.9781560801801

Cowen, J. P., Fornari, D. J., Shank, T. M., Love, B., Glazer, B., Treusch, A. H., Holmes, R. C., et al. (2007). Volcanic eruptions at East Pacific Rise near 9°50′N. *Eos Transactions American Geophysical Union*, *88*(7), 81. https://doi.org/10.1029/2007EO070001

Detrick, R. S., Buhl, P., Vera, E., Mutter, J., Orcutt, J., Madsen, J., & Brocher, T. (1987). Multi-channel seismic imaging of a crustal magma chamber along the East Pacific Rise. *Nature*, *326*(6108), 35–41. https://doi.org/10.1038/326035a0

Dunn, R. A., Toomey, D. R., & Solomon, S. C. (2000). Three-dimensional seismic structure and physical properties of the crust and shallow mantle beneath the East Pacific Rise at 9°30′N. *Journal of Geophysical Research*, *105*(B10), 23,537–23,555. https://doi.org/10.1029/2000JB900210

Escartín, J., Soule, S. A., Fornari, D. J., Tivey, M., Schouten, H., & Perfit, M. R. (2007). Interplay between faults and lava flows in construction of the upper oceanic crust: The East Pacific Rise crest 9°25′–9°58′N. *Geochemistry, Geophysics, Geosystems*, *8*, Q06005. https://doi.org/10.1029/2006GC001399

Fontaine, F. J., Olive, J.-A., Cannat, M., Escartín, J., & Perol, T. (2011). Hydrothermally-induced melt lens cooling and segmentation along the axis of fast- and intermediate-spreading centers. *Geophysical Research Letters*, *38*, L14307. https://doi.org/10.1029/2011GL047798

Fontaine, F. J., Rabinowicz, M., & Cannat, M. (2017). Can high-temperature, high-heat flux hydrothermal vent fields be explained by thermal convection in the lower crust along fast-spreading Mid-Ocean Ridges? *Geochemistry, Geophysics, Geosystems*, *18*, 1907–1925. https://doi.org/10.1002/2016GC006737

Fornari, D. J., Haymon, R. M., Perfit, M. R., Gregg, T. K. P., & Edwards, M. H. (1998). Axial summit trough of the East Pacific Rice 9°–10°N: Geological characteristics and evolution of the axial zone on fast spreading mid-ocean ridge. *Journal of Geophysical Research*, *103*(B5), 9827–9855. https://doi.org/10.1029/98JB00028

Fornari, D. J., Perfit, M. R., Allan, J. F., Batiza, R., Haymon, R., Barone, A., et al. (1988). Geochemical and structural studies of the Lamont seamounts: Seamounts as windows into mantle processes. *Earth and Planetary Science Letters*, *89*, 63–83.

Fornari, D. J., Tivey, M. A., Schouten, H., Perfit, M., Yoerger, D., Bradley, A., et al. (2004). Submarine Lava Flow Emplacement at the East Pacific Rise 9° 50′N: Implications for Uppermost Ocean Crust Stratigraphy and Hydrothermal Fluid Circulation. In C. German, et al. (Eds.), *Thermal Structure of the Ocean Crust and the Dynamics of Hydrothermal Circulation*, AGU Geophysical Monograph (Vol. 148, pp. 187–217). Washington, DC: American Geophysical Union.

Fornari, D. J., Von Damm, K. L., Bryce, J. G., Cowen, J. P., Ferrini, V., Fundis, A., et al. (2012). The East Pacific Rise between 9°N and 10°N: Twenty-five years of integrated, multidisciplinary oceanic spreading center studies. *Oceanography*, *25*(1), 18–43. https://doi.org/10.5670/oceanog.2012.02

Fundis, A. T., Soule, S. A., Fornari, D. J., & Perfit, M. R. (2010). Paving the seafloor: Volcanic emplacement processes during the 2005–2006 eruptions at the fast spreading East Pacific Rise, 9°50N. *Geochemistry, Geophysics, Geosystems*, *11*, Q08024. https://doi.org/10.1029/2010GC003058

Gillis, K. M. (2008). The roof of an axial magma chamber: A hornfelsic heat exchanger. *Geology*, *36*(4), 299–302. https://doi.org/10.1130/G24590A.1

Gomez, O., & Briais, A. (2000). Near-axis seamount distribution and its relationship with the segmentation of the East Pacific Rise and northern Pacific–Antarctic Ridge, 178N–568S. *Earth and Planetary Science Letters*, *175*(3-4), 233–246. https://doi.org/10.1016/S0012-821X(99)00305-2

Gregg, P. M., Lin, J., Behn, M. D., & Montési, L. G. (2007). Spreading rate dependence of gravity anomalies along oceanic transform faults. *Nature*, *448*(7150), 183–187. https://doi.org/10.1038/nature05962

Gudmundsson, A. (1990). Emplacement of dikes, sills and crustal magma chambers at divergent plate boundaries. *Tectonophysics*, *176*(3-4), 257–275. https://doi.org/10.1016/0040-1951(90)90073-H

Gudmundsson, A. (2011). Deflection of dykes into sills at discontinuities and magma-chamber formation. *Tectonophysics*, *500*(1-4), 50–64. https://doi.org/10.1016/j.tecto.2009.10.015

Han, S., Carbotte, S. M., Carton, H., Mutter, J., Aghaei, O., Nedimović, M. R., & Canales, J. P. (2014). Architecture of off-axis magma bodies at EPR 9°37–40′N and implication for oceanic crustal accretion. *Earth and Planetary Science Letters*, *390*, 31–44.

Harding, A. J., Kent, G. M., & Orcutt, J. A. (1993). A multichannel seismic investigation of upper crustal structure at 9°N on the East Pacific Rise: Implications for crustal accretion. *Journal of Geophysical Research*, *98*(B8), 13,925–13,944. https://doi.org/10.1029/93JB00886

Haymon, R. M., Fornari, D. J., Edwards, M. H., Carbotte, S., Wright, D., & Macdonald, K. C. (1991). Hydrothermal vent distribution along the East Pacific Rise crest (9°09′–9°54′N) and its relationship to magmatic and tectonic processes on fast spreading mid-ocean ridges. *Earth and Planetary Science Letters*, *104*, 513–534.

Haymon, R. M., Fornari, D. J., Von Damm, K. L., Lilley, M. D., Perfit, M. R., Edmond, J. M., et al. (1993). Volcanic eruption of the mid-ocean ridge along the East Pacific Rise crest at 9°45′–52′N: Direct submersible observations of seafloor phenomena associated with an eruption event in April, 1991. *Earth and Planetary Science Letters*, *119*, 85–101.

Haymon, R. M., & White, S. M. (2004). Fine-scale segmentation of volcanic/hydrothermal systems along fast-spreading ridge crests. *Earth and Planetary Science Letters*, *226*(3-4), 367–382. https://doi.org/10.1016/j.epsl.2004.08.002

Hebert, L. B., & Montési, L. G. (2011). Melt extraction pathways at segmented oceanic ridges: application to the East Pacific Rise at the Siqueiros transform. *Geophysical Research Letters*, *38*, L11306 https://doi.org/10.1029/2011GL047206.

Hooft, E. E. E., Detrick, R. S., & Kent, G. M. (1997). Seismic structure and indicators of magma budget along the Southern East Pacific Rise. *Journal of Geophysical Research*, *102*(B12), 27,319–27,340. https://doi.org/10.1029/97JB02349

Katz, R. F., Spiegelman, M., & Carbotte, S. M. (2004). Ridge migration, asthenospheric flow and the origin of magmatic segmentation in the global mid-ocean ridge system. *Geophysical Research Letters*, *31*, L15605. https://doi.org/10.1029/2004GL020388

Kelemen, P. B., Shimizu, N., & Salters, V. J. M. (1995). Extraction of mid-ocean-ridge basalt from the upwelling mantle by focused flow of melt in dunite channels. *Nature*, *375*(6534), 747–753. https://doi.org/10.1038/375747a0

Kent, G. M., Harding, A. J., & Orcutt, J. A. (1993a). Distribution of magma beneath the East Pacific Rise between the Clipperton transform and the 9°17′N Deval from forward modeling of common depth point data. *Journal of Geophysical Research*, *98*(B8), 13,945–13,969. https://doi.org/10.1029/93JB00705

Kent, G. M., Harding, A. J., & Orcutt, J. A. (1993b). Distribution of magma beneath the East Pacific Rise near the 9°03′N overlapping spreading center from forward modeling of common depth point data. *Journal of Geophysical Research*, *98*(B8), 13,971–13,995. https://doi.org/10.1029/93JB00706

Kent, G. M., Harding, A. J., Orcutt, J. A., Detrick, R. S., Mutter, J. C., & Buhl, P. (1994). Uniform accretion of oceanic crust south of the Garrett transform at 14°15′S on the East Pacific Rise. *Journal of Geophysical Research*, *99*(B5), 9097–9116. https://doi.org/10.1029/93JB02872

Kent, G. M., Singh, S. C., Harding, A. J., Sinha, M. C., Orcutt, J. A., Barton, P. J., et al. (2000). Evidence from three-dimensional seismic reflectivity images for enhanced melt supply beneath mid-ocean-ridge discontinuities. *Nature*, *406*(6796), 614–618. https://doi.org/10.1038/35020543

Langmuir, C. H., Bender, J. F., & Batiza, R. (1986). Petrological and tectonic segmentation of the East Pacific Rise, 5°30′–14°30′N. *Nature*, *322*(6078), 422–429. https://doi.org/10.1038/322422a0

Le Mée, L., Girardeau, J., & Monnier, C. (2004). Mantle segmentation along the Oman ophiolite fossil mid-ocean ridge. *Nature*, *432*(7014), 167–172. https://doi.org/10.1038/nature03075

Lonsdale, P. (1989). Segmentation of the Pacific-Nazca Spreading Center, 18N–208S. *Journal of Geophysical Research*, *94*, 12,197–12,225.

Macdonald, K. C., Fox, P. J., Carbotte, S., Eisen, M., Miller, S., Penam, L., et al. (1992). The East Pacific Rise and its flanks, 8°–18°N: History of segmentation, propagation and spreading direction based on SeaMARC II and Sea Beam studies. *Marine Geophysical Researches*, *14*(4), 299–344. https://doi.org/10.1007/BF01203621

Macdonald, K. C., Fox, P. J., Perram, L. J., Eisen, M. F., Haymon, R. M., Miller, S. P., et al. (1988). A new view of the mid-ocean ridge from the behaviour of ridge axis discontinuities. *Nature*, *335*(6187), 217–225. https://doi.org/10.1038/335217a0

Macdonald, K. C., Scheirer, D. S., & Carbotte, S. M. (1991). Mid-ocean ridges: Discontinuities, segments and giant cracks. *Science*, *253*(5023), 986–994. https://doi.org/10.1126/science.253.5023.986

Marjanović, M. (2013). Signature of present and past melt distribution at fast and intermediate spreading centers, *PhD thesis*, Columbia University, New York.

Marjanović, M., Carbotte, S. M., Carton, H., Nedimović, M. R., Mutter, J. C., & Canales, J. P. (2014). A multi-sill magma plumbing system beneath the axis of the East Pacific Rise. *Nature Geoscience*, *7*(11), 825–829. https://doi.org/10.1038/ngeo2272

Marjanović, M., Carbotte, S., Mutter, J. C., Nedimović, M., & Canales, J. P. (2018). Processed 3D volume of multichannel seismic data on the East Pacific Rise (9 deg 20 minutes N to 10 deg 10 minutes N), acquired during R/V Marcus G. Langseth expedition MGL10812 (2008). Academic Seismic Portal at UTIG, Marine Geoscience Data System. http://dx.doi.org/10.1594/IEDA/500205

Marjanović, M., Carton, H. D., Nedimović, M. R., Carbotte, S. M., Mutter, J., & Canales, J. P. (2015). Distribution of melt along the East Pacific Rise from 9°30′ to 10°N from an amplitude variation with angle of incidence (AVA) technique. *Geophysical Journal International*, *203*(1), 1–21. https://doi.org/10.1093/gji/ggv251

Marjanović, M., Fuji, N., Singh, S. C., Belahi, T., & Escartín, J. (2017). Seismic signatures of hydrothermal pathways along the East Pacific Rise between 9°16′ and 9°56′N. *Journal of Geophysical Research: Solid Earth*, *122*, 10,241–10,262. https://doi.org/10.1002/2017JB015004

Menand, T. (2008). The mechanics and dynamics of sills in layered elastic rocks and the irimplications for the growth of laccoliths and other igneous complexes. *Earth and Planetary Science Letters*, *267*, 93–99.

Menand, T. (2011). Physical controls and depth of emplacement of igneous bodies: A review. *Tectonophysics*, *500*(1-4), 11–19. https://doi.org/10.1016/j.tecto.2009.10.016

Miller, C. F., Furbish, D. J., Walker, B. A., Claiborne, L. L., Koteas, G. C., Bleick, H. A., & Miller, J. S. (2011). Growth of plutons by incremental emplacement of sheets in crystal-rich host: Evidence from Miocene intrusions of the Colorado River region, Nevada, USA. *Tectonophysics*, *500*(1-4), 65–77. https://doi.org/10.1016/j.tecto.2009.07.011

Momoh, E., Cannat, M., Watremez, L., Leroy, S., & Singh, S. C. (2017). Quasi-3D seismic reflection imaging and wide-angle velocity structure of nearly amagmatic oceanic lithosphere at the ultraslow-spreading Southwest Indian Ridge. *Journal of Geophysical Research: Solid Earth*, *122*, 9511–9533. https://doi.org/10.1002/2017JB014754

Mutter, J., Carbotte, S., Canales, J. and M. Nedimović, (2008). Multi-channel seismic shot data from the East Pacific Rise 9 Degrees North Spreading Center Segment acquired during R/V Marcus G. Langseth expedition MGL0812 (2008). Integrated Earth Data Applications (IEDA) doi:https://doi.org/10.1594/IEDA/314654

Mutter, J. C., Barth, G. A., Buhl, P., Detrick, R. S., Orcutt, J., & Harding, A. (1988). Magma distribution across ridge-axis discontinuities on the East Pacific Rise from multichannel seismic images. *Nature*, *336*(6195), 156–158. https://doi.org/10.1038/336156a0

Mutter, J. C., Carbotte, S. C., Su, W., Xu, L., Buhl, P., Detrick, R. S., et al. (1995). Seismic images of active magma systems beneath the East Pacific Rise between 17°05′ and 17°35′S. *Science*, *268*(5209), 391–395. https://doi.org/10.1126/science.268.5209.391

Natland, J. H., & Dick, H. J. B. (2001). Formation of the lower ocean crust and the crystallization of gabbroic cumulates at a very slowly spreading ridge. *Journal of Volcanology and Geothermal Research*, *110*, 3–4.

Nedimović, M. R., Carbotte, S. M., Diebold, J. B., Harding, A. J., Canales, J. P., & Kent, G. M. (2008). Upper crustal evolution across the Juan de Fuca ridge flanks. *Geochemistry, Geophysics, Geosystems*, *9*, Q09006. https://doi.org/10.1029/2008GC002085

Parsons, T., Sleep, N. H., & Thompson, G. A. (1992). Host rock rheology controls on the emplacement of tabular intrusions: Implications for underplating of extending crust. *Tectonics*, *11*(6), 1348–1356. https://doi.org/10.1029/92TC01105

Phipps Morgan, J., & Chen, Y. J. (1993). The genesis of oceanic crust: Magma injection, hydrothermal circulation, and crustal flow. *Journal of Geophysical Research*, *98*(B4), 6283–6297. https://doi.org/10.1029/92JB02650

Rabinowicz M., Genthon P., Ceuleneer G., & Hillairet M. (2001). Compaction in a mantle mush with high melt concentrations and the generation of magma chambers. *Earth and Planetary Science Letters 188*, 313–328.

Rubin, K. H., Soule, S. A., Chadwick, W. W. Jr., Fornari, D. J., Clague, D. A., Embley, R. W., et al. (2012). Volcanic eruptions in the deep sea. *Oceanography*, *25*(1), 142–157. https://doi.org/10.5670/oceanog.2012.12

Ryan, W. B. F., Carbotte, S. M., Coplan, J. O., O'Hara, S., Melkonian, A., Arko, R., et al. (2009). Global Multi-Resolution Topography synthesis. *Geochemistry, Geophysics, Geosystems*, *10*, Q03014. https://doi.org/10.1029/2008GC002332

Scheirer, D. S., & Macdonald, K. C. (1993). Variation in cross-sectional area of the axial ridge along the East Pacific Rise: Evidence for the magmatic budget of a fast spreading center. *Journal of Geophysical Research*, *98*(B5), 7871–7885. https://doi.org/10.1029/93JB00015

Schouten, H., Tivey, M. A., Fornari, D. J., & Cochran, J. R. (1999). Central Anomaly Magnetization High: Constraints on the volcanic construction and architecture of seismic layer 2A at a fast-spreading Mid-Ocean Ridge, the EPR at 9°30′–50′N. *Earth and Planetary Science Letters*, *169*, 37–50.

Singh, S. C., Harding, A. J., Kent, G. M., Sinha, M. C., Combier, V., Nazin, S., et al. (2006). Seismic reflection images of the Moho underlying melt sill at the East Pacific Rise. *Nature*, *442*(7100), 287–290. https://doi.org/10.1038/nature04939

Singh, S. C., Kent, G. M., Collier, J. S., Harding, A. J., & Orcutt, J. A. (1998). Melt to mush variations in crustal magma properties along the ridge crest at the southern East Pacific Rise. *Nature*, *394*(6696), 874–878. https://doi.org/10.1038/29740

Sinton, J. M., & Detrick, R. S. (1992). Mid-ocean ridge magma chambers. *Journal of Geophysical Research*, *97*(B1), 197–216. https://doi.org/10.1029/91JB02508

Sinton, J. M., Smaglik, S. M., Mahoney, J. J., & Macdonald, K. C. (1991). Magmatic processes at superfast spreading mid-ocean ridges: Glass compositional variations along the East Pacific Rise 138–238S. *Journal of Geophysical Research*, *96*(B4), 6133–6155. https://doi.org/10.1029/90JB02454

Smith, M., Perfit, M. R., Fornari, D. J., Ridley, W. I., Edwards, M. H., Kurras, G., & Von Damm, K. L. (2001). Segmentation and magmatic processes at a fast spreading mid-ocean ridge: Detailed geochemistry and mapping of the East Pacific Rise crest at the 9° 37′N OSC. *Geochemistry, Geophysics, Geosystems*, *2*. https://doi.org/10.1029/2000GC000134

Soule, S. A., Escartin, J., & Fornari, D. J. (2009). A record of eruption and intrusion at a fast spreading ridge axis: Axial summit trough of the East Pacific Rise 9–10°N. *Geochemistry, Geophysics, Geosystems*, *10*, Q10T07. https://doi.org/10.1029/2008GC002354

Soule, S. A., Fornari, D. J., Perfit, M. R., & Rubin, K. (2007). New insights into mid-ocean ridge volcanic processes from the 2005–2006 eruption of the East Pacific Rise, 9°46′N–9°56′N. *Geology*, *35*(12), 1079–1082. https://doi.org/10.1130/G23924A.1

Soule, S. A., Fornari, D. J., Perfit, M. R., Tivey, M. A., Ridley, W. I., & Schouten, H. (2005). Channelized lava flows at the East Pacific Rise crest 9–10°N: The importance of off-axis lava transport in developing the architecture of young oceanic crust. *Geochemistry, Geophysics, Geosystems*, *6*, 008005. https://doi.org/10.1029/2005GC000912

Taisne, B., & Jaupart, C. (2009). Dike propagation through layered rocks. *Journal of Geophysical Research*, *114*, B09203. https://doi.org/10.1029/2008JB006228

Tan, Y. J., Tolstoy, M., Waldhauser, F., & Wilcock, W. S. (2016). Dynamics of a seafloor-spreading episode at the East Pacific Rise. *Nature*, *540*(7632), 261–265. https://doi.org/10.1038/nature20116

Tolstoy, M., Cowen, J. P., Baker, E. T., Fornari, D. J., Rubin, K. H., Shank, T. M., et al. (2006). A sea-floor spreading event captured by seismometers. *Science*, *314*(5807), 1920–1922. https://doi.org/10.1126/science.1133950

Tolstoy, M., Waldhauser, F., Bohnenstiehl, D. R., Weekly, R. T., & Kim, W.-Y. (2008). Seismic identification of along-axis hydrothermal flow on the East Pacific Rise. *Nature*, *415*, 181–184.

Toomey, D., & Hooft, E. E. E. (2008). Mantle upwelling, magmatic differentiation, and the meaning of axial depth at fast-spreading ridges. *Geology*, *36*(9), 679–682. https://doi.org/10.1130/G24834A.1

Toomey, D., Jousselin, D., Dunn, R., Wilcock, W., & Detrick, R. (2017). Shallow mantle seismic velocity structure at the East Pacific Rise between 8–10N. Data set. Integrated Earth Data Applications (IEDA). https://doi.org/10.1594/IEDA/324051

Toomey, D. R., Jousselin, D., Dunn, R. A., Wilcock, W. S. D., & Detrick, R. S. (2007). Skew of mantle upwelling beneath the East Pacific Rise governs segmentation. *Nature*, *446*(7134), 409–414. https://doi.org/10.1038/nature05679

VanderBeek, B., Toomey, D. R., Hooft, E. E. E., & Willcock, W. S. D. (2016). Segmentation of mid-ocean ridges attributed to oblique mantle divergence. *Nature Geoscience*, *9*(8), 636–642. https://doi.org/10.1038/ngeo2745

Vera, E. E., & Diebold, J. B. (1994). Seismic imaging of oceanic layer 2A between 9°30′N and 10°N on the East Pacific Rise from two-ship wide-aperture profiles. *Journal of Geophysical Research*, *99*(B2), 3031–3041. https://doi.org/10.1029/93JB02107

Vera, E. E., Mutter, J. C., Buhl, P., Orcutt, J. A., Harding, A. J., Kappus, M. E., et al. (1990). The structure of 0- to 0.2-m.y.-old oceanic crust at 9°N on the East Pacific Rise from expanded spread profiles. *Journal of Geophysical Research*, *95*(B10), 15,529–15,556.

Von Damm, K. L. (1995). Controls on the chemistry and temporal variability of seafloor hydrothermal fluids. In S. E. Humphris, R. A. Zierenberg, L. S. Mullineaux, & R. E. Thompson (Eds.), *Seafloor hydrothermal systems: Physical, chemical, biologic and geologic interactions*, *Geophysical Monograph Series*, (Vol. 91, pp. 222–248). Washington, D. C: American Geophysical Union.

Von Damm, K. L. (2000). Chemistry of hydrothermal vent fluids from 9-10N, East Pacific Rise: "Time zero," the immediate posteruptive period. *Journal of Geophysical Research*, *105*(B5), 11,203–11,222.

Von Damm, K. L. (2004). Evolution of the hydrothermal system at East Pacific Rise 9°50′N: Geochemical evidence for changes in the upper oceanic crust. In C. R. German, J. Lin, & L. M. Parson (Eds.), *Hydrothermal interactions between the lithosphere and oceans*, *Geophysical Monograph Series*, (Vol. 148, pp. 285–305). Washington, DC: American Geophysical Union.

Wang, X., Cochran, J. R., & Barth, G. (1996). Gravity anomalies, crustal thickness and the pattern of mantle flow at the fast spreading East Pacific Rise, 9°N–10°N: Evidence for three-dimensional upwelling. *Journal of Geophysical Research*, *101*(B8), 17,927–17,940. https://doi.org/10.1029/96JB00194

White, S. M., Haymon, R. M., & Carbotte, S. (2006). A new view of ridge segmentation and near-axis volcanism at the East Pacific Rise, 8–12°N, from EM300 multibeam bathymetry. *Geochemistry, Geophysics, Geosystems*, *7*, Q12O05. https://doi.org/10.1029/2006GC001407

White, S. M., Haymon, R. M., Fornari, D. J., Perfit, M. R., & Macdonald, K. C. (2002). Correlation between volcanic and tectonic segmentation of fast-spreading ridges: Evidence from volcanic structures and lava flow morphology on the East Pacific Rise at 9°–10°N. *Journal of Geophysical Research*, *107*(B8), 2173. https://doi.org/10.1029/2001JB000571

White, S. M., Macdonald, K. C., & Haymon, R. M. (2000). Basaltic lava domes, lava lakes, and volcanic segmentation on the southern East Pacific Rise. *Journal of Geophysical Research*, *105*(B10), 23,519–23,536. https://doi.org/10.1029/2000JB900248

Xu, M., Canales, J. P., Carbotte, S. M., Carton, H., Nedimović, M. R., & Mutter, J. C. (2014). Variations in axial magma lens properties along the East Pacific Rise (9°30′–10°00′N) from swath 3D seismic imaging and 1D waveform inversion. *Journal of Geophysical Research: Solid Earth*, *119*, 2721–2744. https://doi.org/10.1002/2013JB010730

Yilmaz, O. (2001). *Seismic data analysis, processing, inversion, and interpretation of seismic data*. Tulsa: Society of Exploration Geophysicists. https://doi.org/10.1190/1.9781560801580